

Magnetism, superconductivity, and spontaneous orbital order in iron-based superconductors: who comes first and why?

Andrey V. Chubukov¹, M. Khodas^{2,3}, and Rafael M. Fernandes¹

¹ *School of Physics and Astronomy,*

University of Minnesota, Minneapolis, MN 55455, USA

² *Racah Institute of Physics, The Hebrew University, Jerusalem 91904, Israel*

³ *Department of Physics and Astronomy,*

University of Iowa, Iowa City, IA 52242, USA

Abstract

Magnetism and nematic order are the two non-superconducting orders observed in iron-based superconductors. To elucidate the interplay between them and ultimately unveil the pairing mechanism, several models have been investigated. In models with quenched orbital degrees of freedom, magnetic fluctuations promote stripe magnetism which induces orbital order. In models with quenched spin degrees of freedom, charge fluctuations promote spontaneous orbital order which induces stripe magnetism. Here we develop an unbiased approach, in which we treat magnetic and orbital fluctuations on equal footing. Key to our approach is the inclusion of the orbital character of the low-energy electronic states into renormalization group analysis. Our results show that in systems with large Fermi energies, such as BaFe_2As_2 , LaFeAsO , and NaFeAs , orbital order is induced by stripe magnetism. However, in systems with small Fermi energies, such as FeSe , the system develops a spontaneous orbital order, while magnetic order does not develop. Our results provide a unifying description of different iron-based materials.

Introduction. The interplay between magnetism and orbital order and how the two affect superconductivity are the most interesting, yet, most controversial aspects of the physics of iron-based superconducting materials (FeSCs). Both orbital and magnetic fluctuations have been proposed as the glue that binds electrons together for superconductivity, yielding different pairing states [1–8]. However, which of the two degrees of freedom, orbital or spin, is the driving force, is a hotly debated topic [9–22].

The proponents of either orbital or magnetic fluctuations put forward models in which the unwanted degree of freedom is quenched. In a class of models where spin degrees of freedom are quenched [6, 8, 23], density fluctuations with opposite signs on the Fe d_{xz} and d_{yz} orbitals are enhanced as the temperature is lowered. Consequently, below a temperature T_s the occupation of the d_{xz} and d_{yz} orbitals becomes unequal, breaking the tetragonal symmetry of the system and triggering a structural transition. This orbital order can either be homogeneous (ferro-orbital order) or with a lattice wavevector (antiferro-orbital order (AFO)). In the band basis, ferro-orbital order is a Pomeranchuk-type (POM) order in the d -wave charge channel [24]. Such an order has been extensively studied in recent years in the context of quantum criticality [8, 25]. Orbital fluctuations can mediate superconductivity (SC) and favor a sign-preserving s^{++} SC order [1, 6, 8].

In models where orbital degrees of freedom are quenched, orbital order is a spin-off of stripe spin-density-wave (SDW) magnetism. Stripe SDW order breaks the tetragonal symmetry between the x and y directions in addition to breaking the spin-rotational symmetry [26]. It has been shown [9, 17] that the breaking of the discrete tetragonal symmetry occurs prior to the breaking of the continuous spin-rotational symmetry, via the development of a composite Ising-nematic order. By symmetry arguments, this order induces orbital order [27]. Magnetic fluctuations that drive Ising-nematic order also favor a sign-changing s^{+-} SC [2, 3, 5, 9, 28].

Each set of models uses approximations which have been strongly questioned. Orbital models assume attractive local (Hubbard) intra-pocket interaction, in variance with first-principle calculations [29]. Magnetic models either assume a priori that superconductivity is magnetically mediated [4], or treat superconductivity and magnetism on equal footing, but neglect the orbital content of low-energy excitations [32, 33]. In reality, however, magnetic and orbital degrees of freedom are coupled and affect each other [30, 31].

In this work we treat magnetism, superconductivity, and orbital order on equal footing.

We use the renormalization group (RG) technique, which is the most unbiased way to analyze how different interaction channels affect each other and what is the leading (and the subleading) instability in the system [32, 33, 36–39]. We list potential instabilities in Fig. 1 and show how each reconstructs the fermionic states. We consider a model with repulsive intra-pocket interaction, like in earlier studies of the interplay between magnetism and superconductivity. However, in distinction to earlier works [17, 32, 33] we explicitly include into consideration the orbital composition of the low-energy electronic states. This allows us to consider fluctuations in the orbital channel on equal footing with fluctuations in the magnetic and superconducting channels. We assume that there is a substantial energy range of metallic behavior and do not discuss Hund metallic behavior [34] and orbitally-selective Mottness [35].

The two key questions we address are: (i) How one can get an attraction in the orbital channel out of purely repulsive bare interactions? (ii) If the orbital channel is attractive, can orbital order develop, upon lowering the temperature, prior to magnetism and superconductivity?

We show that the outcome depends on whether the leading instability develops at a temperature T_{ins} smaller or larger than the Fermi energy E_F . When $T_{\text{ins}} < E_F$, the orbital composition of the low-energy excitations does not play a crucial role and the system develops either SDW and Ising-nematic order or s^{+-} SC order. This is the case for most iron-based systems. However, when $T_{\text{ins}} > E_F$, which is the case of FeSe, the orbital composition is crucial, and the d -wave POM instability occurs prior to the SDW and SC instabilities, giving rise to a spontaneous orbital order. This orbital order, however, is not the consequence of a strong attraction in the POM channel at the bare (mean-field) level. Instead, the instability in the POM channel is induced and pushed to a higher temperature by magnetic fluctuations, which take advantage of the repulsive electronic interactions of the system. At the same time, this magnetically-driven Pomeranchuk instability is very different from the Ising-nematic instability, because it is not a vestige of a stripe magnetic order.

The interplay between SDW, SC, and POM orders in FeSCs has been earlier analyzed numerically using functional RG (fRG) approach [37–39], and the POM channel was found to be a distant third, after SDW and SC. This conclusion, however, follows from comparative analysis of the running couplings in different channels. We argue that the analysis of the couplings is insufficient, and to analyze which channel becomes unstable first, one has to

compare the corresponding susceptibilities. This is how POM channel comes ahead of SC and SDW channels. We use analytical parquet RG (pRG), which allows us to analyze the flow not only of the couplings, but also of susceptibilities.

The Model We depart from the actual underlying 2D microscopic model in the orbital basis. The kinetic energy is given by the hopping terms involving all five Fe-orbitals (direct and via pnictogen/chalcogen sites) and the potential energy describes onsite interactions between the Fe-orbitals. These interactions include intra-orbital and inter-orbital Hubbard and Hund terms (Refs. [3, 4, 34]). We convert from orbital into band basis and obtain the corresponding band model. The orbital composition of the excitations does not show up in the kinetic part of the Hamiltonian in the band basis, but it imposes angular dependencies on the four-fermion interaction terms. As we will show, the terms with different angular dependencies flow differently under pRG.

The fermionic structure in the band basis contains hole and electron pockets. Two hole pockets are centered at the Γ point ($k_x = k_y = 0$) and are constructed out of d_{xz} and d_{yz} orbitals (Fig. 1). In some materials there exists another hole pocket, centered at (π, π) in the 1-Fe zone and made fully out of d_{xy} orbital [40]. This pocket will not play a role in our analysis and we neglect it. The Fourier components of the d_{xz} and d_{yz} operators with momenta k near Γ are related to c_k and d_k operators describing excitations near the two Γ -centered hole pockets by a rotation [41]

$$d_{xz,k} = \cos \theta_k c_k + \sin \theta_k d_k, \quad d_{yz,k} = \cos \theta_k d_k - \sin \theta_k c_k, \quad (1)$$

The rotation angle θ_k coincides with the angle along the hole Fermi surface if the hole pockets can be approximated as circular, which we assume to be the case. The extension to a more general Fermi surface geometry complicates the formulas but does not introduce new physics. The kinetic energy in the band basis is $\mathcal{H}_{2,h} = \sum_k \epsilon_{c,k} c_k^\dagger c_k + \epsilon_{d,k} d_k^\dagger d_k$, where $\epsilon_{c,k} = \mu - k^2/(2m_c)$ and $\epsilon_{d,k} = \mu - k^2/(2m_d)$, with k near the Γ point. The two dispersions are not identical when $m_c \neq m_d$, but are degenerate by symmetry at $k = 0$ in the absence of spin-orbit coupling [41]. The degeneracy implies that both Γ -centered hole pockets *must be present simultaneously already in the minimal model*.

The two electron pockets are centered at $Q_1 = (0, \pi)$ and $Q_2 = (\pi, 0)$ in the 1-Fe Brillouin zone (Fig. 1). The kinetic energy of the fermions near the electron pockets is $\mathcal{H}_{2,e} = \sum_k \epsilon_{f_1,k} f_{1,k}^\dagger f_{1,k} + \epsilon_{f_2,k} f_{2,k}^\dagger f_{2,k}$, where $\epsilon_{f_1,k} = \epsilon_0 + k_x^2/(2m_x) + k_y^2/(2m_y) - \mu$ and $\epsilon_{f_2,k} = \epsilon_0 +$

$k_x^2/(2m_y) + k_y^2/(2m_x) - \mu$, with k measured with respect to Q_i for $f_{i,k} \equiv f_{i,k+Q_i}$. The two electron pockets are related by C_4 symmetry and transform into each other under a $\pi/2$ rotation. The band fermions $f_{1,k+Q_1}$ and $f_{2,k+Q_2}$ are linear combinations of d_{xz}/d_{xy} and d_{yz}/d_{xy} orbitals, respectively [3, 4], and the relative amplitude of the spectral weights depends on system parameters.

The interactions between low-energy fermions are Hubbard and Hund terms expressed via corresponding band operators. Although there are only four interactions at the bare level (U, U', J, J'), the number of topologically distinct invariant combinations of 4-fermion terms is much higher and equals 30 for a generic 4-band model in the absence of spin-orbit coupling [41]. The bare values of all 30 couplings are expressed in terms of U, U', J, J' , but under pRG the couplings flow to different values. To make the problem analytically treatable, we neglect the d_{xy} spectral weight on the electron pockets, i.e. we identify the excitations near the $(0, \pi)$ ($(\pi, 0)$) pocket with the d_{xz} (d_{yz}) orbital, $f_{1,k+Q_1} = d_{xz,k+Q_1}$ and $f_{2,k+Q_2} = d_{yz,k+Q_2}$. This approximation reduces the number of couplings to manageable 14. As a verification, we considered the opposite case, when we kept only the d_{xy} spectral weight on the two electron pockets. We obtained the same results as with pure d_{xz} (d_{yz}) pockets. This gives us confidence that the approximation we make does not change the physics.

The 14 different interaction parameters are the prefactors for 14 combinations of the original 152 interaction terms in the band basis (96 involving c and d fermions, 8 involving f_1 and f_2 fermions, and 48 cross-terms), combined using the symmetry condition that under rotation by $\pi/2$, $c_k \rightarrow -d_k$, $d_k \rightarrow c_k$, and $f_1 \rightarrow f_2$. We present the full form of the interaction term \mathcal{H}_4 in the Supplementary Material (SM), and here show a representative set from each

combination:

$$\begin{aligned}
\mathcal{H}_4 = & \sum_{k_i} c_{k_1,\alpha}^\dagger f_{1;k_2,\beta}^\dagger f_{1;k_3,\beta} c_{k_4,\alpha} \left[U_1 \cos \theta_{\mathbf{k}_1} \cos \theta_{\mathbf{k}_4} + \bar{U}_1 \sin \theta_{\mathbf{k}_1} \sin \theta_{\mathbf{k}_4} \right] \\
& + \sum_{k_i} c_{k_1,\alpha}^\dagger f_{1;k_2,\beta}^\dagger c_{k_3,\beta} f_{1;k_4,\alpha} \left[U_2 \cos \theta_{\mathbf{k}_1} \cos \theta_{\mathbf{k}_3} + \bar{U}_2 \sin \theta_{\mathbf{k}_1} \sin \theta_{\mathbf{k}_3} \right] \\
& + \sum_{k_i} c_{k_1,\alpha}^\dagger c_{k_2,\beta}^\dagger f_{1;k_3,\beta} f_{1;k_4,\alpha} \left[\frac{U_3}{2} \cos \theta_{\mathbf{k}_1} \cos \theta_{\mathbf{k}_2} + \frac{\bar{U}_3}{2} \sin \theta_{\mathbf{k}_1} \sin \theta_{\mathbf{k}_2} \right] \\
& + \sum_{k_i} c_{k_1,\alpha}^\dagger c_{k_2,\beta}^\dagger c_{k_3,\beta} c_{k_4,\alpha} \left[\frac{U_4}{2} \cos \theta_{\mathbf{k}_1} \cos \theta_{\mathbf{k}_2} \cos \theta_{\mathbf{k}_3} \cos \theta_{\mathbf{k}_4} + \frac{\bar{U}_4}{2} \cos \theta_{\mathbf{k}_1} \cos \theta_{\mathbf{k}_2} \sin \theta_{\mathbf{k}_3} \sin \theta_{\mathbf{k}_4} \right] \\
& + \sum_{k_i} c_{k_1,\alpha}^\dagger c_{k_2,\beta}^\dagger c_{k_3,\beta} c_{k_4,\alpha} \left[\tilde{U}_4 \cos \theta_{\mathbf{k}_1} \sin \theta_{\mathbf{k}_2} \sin \theta_{\mathbf{k}_3} \cos \theta_{\mathbf{k}_4} + \tilde{\tilde{U}}_4 \cos \theta_{\mathbf{k}_1} \sin \theta_{\mathbf{k}_2} \cos \theta_{\mathbf{k}_3} \sin \theta_{\mathbf{k}_4} \right] \\
& + \sum_{k_i} \frac{U_5}{2} f_{1;k_1,\alpha}^\dagger f_{1;k_2,\beta}^\dagger f_{1;k_3,\beta} f_{1;k_4,\alpha} + \frac{\bar{U}_5}{2} f_{1;k_1,\alpha}^\dagger f_{1;k_2,\beta}^\dagger f_{2;k_3,\beta} f_{2;k_4,\alpha} \\
& + \sum_{k_i} \tilde{U}_5 f_{1;k_1,\alpha}^\dagger f_{2;k_2,\beta}^\dagger f_{2;k_3,\beta} f_{1;k_4,\alpha} + \tilde{\tilde{U}}_5 f_{1;k_1,\alpha}^\dagger f_{2;k_2,\beta}^\dagger f_{1;k_3,\beta} f_{2;k_4,\alpha} + \dots
\end{aligned} \tag{2}$$

where ... stand for other terms in each of the 14 combinations in (2). Out of the 14 interactions, 4 are density-density, exchange and pair-hopping terms for fermions near the two hole pockets ($U_4, \bar{U}_4, \tilde{U}_4, \tilde{\tilde{U}}_4$), another 4 are analogous interactions for fermions near the two electron pockets ($U_5, \bar{U}_5, \tilde{U}_5, \tilde{\tilde{U}}_5$), and 6 involve fermions near both hole and electron pockets ($U_1, \bar{U}_1, U_2, \bar{U}_2, U_3, \bar{U}_3$). The bare values of these 14 couplings are $U_1 = U_2 = U_3 = U_4 = U_5 = U$, $\bar{U}_1 = \tilde{U}_4 = \tilde{\tilde{U}}_5 = U'$, $\bar{U}_2 = \tilde{U}_4 = \tilde{\tilde{U}}_5 = J$, $\bar{U}_3 = \bar{U}_4 = \bar{U}_5 = J'$.

RG equations In the mean-field approach the bare values of these 14 couplings are used to compute susceptibilities in SDW, SC, POM and other channels. A simple analysis shows that in mean-field, SDW wins over SC and orbital order. However, the mean-field approach is strongly questionable because it effectively isolates each electronic channel, neglecting their interplay and mutual feedback. To overcome this limitation, here we implement a pRG approach and calculate how the couplings and the susceptibilities in different channels evolve as high-energy degrees of freedom are integrated out. In this approach, each dimensionless coupling $u_i = (A_i/4\pi)U_i$, where A_i are combinations of effective masses, acquires a dependence on the running energy/temperature scale E via $L = \log W/E$, where W is of the order of the bandwidth.

The derivation of the one-loop RG equations is tedious but straightforward. We present the details and the full equations in the SM and here list the 14 pRG equations in the

approximation $m_c = m_d = m_h, m_x = m_y = m_e$:

$$\begin{aligned}
\dot{u}_1 &= u_1^2 + u_3^2/C^2, \quad \dot{\bar{u}}_1 = \bar{u}_1^2 + \bar{u}_3^2/C^2, \quad \dot{u}_2 = 2u_1u_2 - 2u_2^2, \quad \dot{\bar{u}}_2 = 2\bar{u}_1\bar{u}_2 - 2\bar{u}_2^2 \\
\dot{u}_3 &= -u_3u_4 - \bar{u}_3\bar{u}_4 + 4u_3u_1 - u_5u_3 - u_8\bar{u}_3 - 2u_2u_3, \quad \dot{\bar{u}}_3 = -\bar{u}_3u_4 - u_3\bar{u}_4 + 4\bar{u}_3\bar{u}_1 - u_5\bar{u}_3 - u_8u_3 - 2\bar{u}_2\bar{u}_3 \\
\dot{u}_4 &= -u_4^2 - \bar{u}_4^2 - u_3^2 - \bar{u}_3^2, \quad \dot{\bar{u}}_4 = -2u_4\bar{u}_4 - 2u_3\bar{u}_3, \quad \dot{u}_5 = -u_5^2 - u_8^2 - u_3^2 - \bar{u}_3^2, \quad \dot{\bar{u}}_5 = -2u_5\bar{u}_5 - 2u_3\bar{u}_3 \\
\dot{\tilde{u}}_4 &= -(\tilde{u}_4^2 + \tilde{\bar{u}}_4^2), \quad \dot{\tilde{\bar{u}}}_4 = -2\tilde{u}_4\tilde{\bar{u}}_4, \quad \dot{\tilde{u}}_5 = -(\tilde{u}_5^2 + \tilde{\bar{u}}_5^2), \quad \dot{\tilde{\bar{u}}}_5 = -2\tilde{u}_5\tilde{\bar{u}}_5
\end{aligned} \tag{3}$$

where $C = (m_e + m_h)/(2\sqrt{m_em_h})$.

One can immediately verify that the running couplings flow to different values under the pRG, and these new values *cannot* be re-expressed just in terms of running U, U', J, J' . As a consequence, the model with only local interactions does not survive under renormalization and longer-range interactions emerge in the process of pRG flow. The minimal model with 14 couplings includes all symmetry-allowed interactions within a plaquette of four Fe atoms. We present the corresponding Hamiltonian in the SM.

RG flow The analysis of Eq. (3) readily reveals that the last four RG equations decouple from the other ten, and that $\tilde{u}_{4,5}$ and $\tilde{\bar{u}}_{4,5}$ flow to zero under pRG. The remaining ten pRG equations are all coupled and have to be solved self-consistently. For $U' = J = J' = 0$, the bare values of the couplings \bar{u}_i ($i = 1 - 5$) are zero, and a straightforward analysis of Eq. (3) shows that they remain zero under pRG. This leads to the same system behavior as found in previous studies [33]. However, the solution with $\bar{u}_i = 0$ becomes unstable already for arbitrarily small U', J and J' , i.e. for arbitrarily small bare \bar{u}_i . We have analyzed the pRG equations for non-zero bare \bar{u}_i and found that the system flows towards a single stable fixed trajectory, along which u_i and \bar{u}_i become equivalent. This implies that the terms \bar{u}_i , which were originally of order U' or even J , grow under pRG and eventually become comparable to u_i , which were originally of order U . In other words, the initial hierarchy of interactions disappears under the pRG flow towards the fixed trajectory [42]. We show the RG flow in Fig. 2.

Along the stable fixed trajectory, the ratios between various couplings become pure numbers: $u_2 = \gamma_2 u_1$, $u_3 = \bar{u}_3 = \gamma_3 u_1$, $u_4 = \bar{u}_4 = \gamma_4 u_1$, $u_5 = \bar{u}_5 = \gamma_5 u_1$. Solving (3) for u_1 and γ_i we obtain

$$\begin{aligned}
u_1 &= \frac{a}{(L_0 - L)}, \quad a = 1/(8C^2 + 4\sqrt{1 - C^2 + 4C^4}), \quad \gamma_2 = \bar{\gamma}_2 = 0, \\
\gamma_3 &= C\sqrt{8C^2 - 1 + 4\sqrt{1 - C^2 + 4C^4}}, \quad \gamma_4 = \gamma_5 = 1 - 2C^2 - \sqrt{1 - C^2 + 4C^4}
\end{aligned} \tag{4}$$

For $C = 1$, which corresponds to perfect nesting, we have $\gamma_3 = \sqrt{15}$ and $\gamma_4 = -3$. The couplings diverge at the logarithmic scale $L = L_0 = O(W/U) \gg 1$, whose exact value depends on U, U' and J . Note that $\gamma_4 = \gamma_5$ is negative for arbitrary C , hence the couplings u_4 and u_5 necessary change sign under the pRG and become negative along the fixed trajectory. We emphasize that the RG equations are valid up to $L_F = \log W/E_F$, where E_F is the *largest* of the Fermi energies. For $E < E_F$, particle-particle and particle-hole channels no longer “talk” to each other and the flow equation is different (see below).

Competition between channels We now use the results for the pRG flow to find which of the many electronic channels becomes unstable first upon lowering the running energy E , which from physics perspective is equivalent to lowering the temperature T . For this we introduce infinitesimally small vertices $\Gamma_{0,i}$ for the coupling between fermions and order parameters in different channels ($i = \text{SDW, SC, POM, or AFO}$), and identify the combinations of the couplings U^i which renormalize $\Gamma_i^{(0)}$ into $\Gamma_i = \Gamma_i^{(0)}(1 + U^i \Pi_i + \dots)$, where Π_i are the corresponding polarization bubbles. We present the details in SM and list U^i in Table I.

Earlier pRG and fRG studies assumed that the channel with the largest U^i along the fixed trajectory wins. We argue that this procedure is incomplete, and to compare different channels one actually needs to obtain and solve another set of pRG equations for Γ_i , then compute the corresponding susceptibilities, find which ones diverge, and compare the exponents. The leading instability will be in the channel in which the exponent is the largest. This procedure has been applied to the one-band Hubbard model [43] and bi-layer graphene [44], but has not yet been applied to FeSCs. The advantage of using analytical pRG in this procedure is that the RG equations for Γ_i and for the susceptibilities can be obtained in a straightforward way.

The analysis of the susceptibilities is different for the SC/SDW channels and the POM channel. For the SC and SDW channels, Π_i is logarithmic, and, to logarithmic accuracy,

$$\chi_{\text{SDW}}(L) \propto \int_L dL' \Gamma_{\text{SDW}}^2(L'), \quad \chi_{\text{SC}} = \int_L dL' \left(\Gamma_{\text{SC}}^{s+-} \right)^2(L'), \quad (5)$$

where $\Gamma_{\text{SDW}}(L')$ and $\Gamma_{\text{SC}}^{s+-}(L')$ are the fully renormalized SDW and SC vertices obtained from the solutions of pRG equations $\dot{\Gamma}_i \propto \Gamma_i U^i$. We derive these equations in the SM and present them here for the couplings along the fixed trajectory:

$$\dot{\Gamma}_{\text{SDW}} = \Gamma_{\text{SDW}} u_1 \left(1 + \frac{\gamma_3}{C} \right), \quad \dot{\Gamma}_{\text{SC}} = \Gamma_{\text{SC}} u_1 (2\gamma_3 + 2|\gamma_4|), \quad (6)$$

where $\gamma_{3,4}$ are given by (4). Solving these two equations and substituting the results into (5) we obtain

$$\chi_{\text{SDW}}(L) \propto \frac{1}{(L_0 - L)^{\alpha_{\text{SDW}}}}, \quad \chi_{\text{SC}}(L) \propto \frac{1}{(L_0 - L)^{\alpha_{\text{SC}}}} \quad (7)$$

with the exponents

$$\alpha_{\text{SDW}} = 2 \frac{1 + \gamma_3/C}{1 + \gamma_3^2/C^2} - 1, \quad \alpha_{\text{SC}} = 4 \frac{|\gamma_4| + \gamma_3}{1 + \gamma_3^2/C^2} - 1. \quad (8)$$

In Fig. 2a we plot α_i as a function of $C = (m_e + m_h)/(2\sqrt{m_e m_h}) \geq 1$. We see that for all values of C , $1 > \alpha_{\text{SC}} > 0$, while $\alpha_{\text{SDW}} < 0$. This implies that only SC order develops. SDW order does not develop, despite that at the bare level SDW channel was the only attractive channel. We show the behavior of the susceptibilities in SDW and SC (s^{+-}) channels along the fixed trajectory in Fig. 2b.

The phenomenon in which SDW interaction pushes up superconductivity but by itself gets cut by the feedback effect from the rising superconducting fluctuations had already been found in earlier pRG and fRG studies of multi-band FeSCs [33, 38] as well as in pRG and fRG analysis of doped graphene [45, 46]. In our case this effect is additionally enhanced because α_{SC} contains contributions from u_1 , u_3 and \bar{u}_1 , \bar{u}_3 , hence the factor of 2 in front of γ -dependent term in (8), while α_{SDW} contains contributions only from u_3 and u_4 , but not \bar{u}_3 and \bar{u}_4 .

We now turn to the POM channel. Here the situation is different because the particle-hole polarization bubble at energy E is determined by fermions with energies of order E . As a result, within one-loop, s-wave (s^{+-}) and d-wave Pomeranchuk susceptibilities obey algebraic rather than differential equations (see SM) and behave as

$$\chi_{\text{POM}}^s \propto \frac{1}{1 - u_1(4C + |\gamma_4|)} = \frac{1}{L_{P_s} - L}, \quad \chi_{\text{POM}}^d \propto \frac{1}{1 - u_1|\gamma_4|} = \frac{1}{L_{P_d} - L}. \quad (9)$$

For both susceptibilities, the exponent $\alpha_{\text{POM}} = 1$ is larger than $\alpha_{\text{SC}} < 1$. Furthermore, for all values of C , L_{P_s} are smaller than L_0 (for $C = 1$, $L_{P_s} = L_0 - 7/16$, $L_{P_d} = L_0 - 3/8$). As a result, within one-loop pRG, *the first instability upon lowering the temperature actually occurs in the Pomeranchuk channel*. We show the behavior of the susceptibilities in SDW, SC (s^{+-}) and POM channels in Fig. 2b.

Note that at $L = L_{P_{s,d}}$, $u_1 \sim 1$, and the corrections to one-loop pRG may become relevant. Still, the comparison of the susceptibilities clearly favors the POM channel over SC and SDW

channels. Also, number-wise, for $L = L_{P_d}$ and $C = 1$, $u_1 = (1/16)/(L_0 - L) = 1/6$, which is still a small number.

Of the two Pomeranchuk susceptibilities, the larger one is in the s^{+-} (A_{1g}) channel. An order of this kind splits the chemical potentials on hole and electron pockets, but conserves the total number of carriers. Because this does not correspond to a true symmetry breaking, the divergence of χ_{POM}^s must be softened by terms beyond RG, such as the fermionic self-energy [47]. Yet, the relative chemical potential shift $\mu_h - \mu_e$ must be enhanced near the temperature at which χ_{POM}^s diverges within the RG. Interestingly, the analysis of ARPES data for several FeSCs did find [48] some evidence for temperature-dependent $\mu_h - \mu_e$.

The true Pomeranchuk instability is in the d -wave (B_{1g}) channel, signaled by the divergence of χ_{POM}^d . This instability implies that the mean-values of $\Delta_{1h} = \sum_k \langle c_k^\dagger c_k - d_k^\dagger d_k \rangle \cos 2\theta_k$, $\Delta_{2h} = \sum_k \langle c_k^\dagger d_k + d_k^\dagger c_k \rangle \sin 2\theta_k$, and $\Delta_e = \sum_k \langle f_{1,k+Q_1}^\dagger f_{1,k+Q_1} \rangle = -\sum_k \langle f_{2,k+Q_2}^\dagger f_{2,k+Q_2} \rangle$ become non-zero. The solution of the set of coupled equations for Δ_{1h} , Δ_{2h} , and Δ_e at $L = L_{P_d}$ yields $\Delta_{1h} = \Delta_{2h} = 4\Delta_e$ (see SM). Converting these results to the orbital basis, we find that $\langle d_{xz}^\dagger d_{xz} \rangle - \langle d_{yz}^\dagger d_{yz} \rangle$ becomes non-zero, while the cross term $\langle d_{xz}^\dagger d_{yz} + d_{yz}^\dagger d_{xz} \rangle$ remains zero. This corresponds precisely to ferro-orbital order. We emphasize that the origin of this ferro-orbital order is not just an attraction in the POM channel, as proposed by other works. In our case the bare interaction well may be repulsive (when $U + J > 2U'$, see above), yet the POM channel becomes attractive in the process of pRG flow and eventually wins over SC and SDW. The attraction in POM channel is driven by the coupling to magnetic fluctuations, and in this respect the pRG scenario or orbital ordering falls into the orbit of “magnetic scenarios”.

Therefore, the full one-loop pRG analysis shows that the system first develops a ferro-orbital order at T_s and then becomes a superconductor at a lower T_c . SDW order does not develop. This sequence of transitions is fully consistent with that in FeSe. In other FeSCs, however, the system does develop SDW order at T_N at small dopings, and the nematic transition line follows T_N , suggesting that nematic order is a vestige of the SDW order.

To understand this difference between FeSe and other FeSCs, we note that in our analysis we assumed that the pRG flow reaches the fixed trajectory at $L = L_{P_d} \approx L_0$, before the pRG analysis breaks down at an energy comparable to the largest E_F in the system, i.e., at $L = L_F$. This holds when $L_0 < L_F$, i.e., when *all* Fermi energies are small. If $L_F < L_0$, the pRG flow runs up only to $L = L_F$, and at larger L the particle-hole and particle-

particle channels decouple from each other. As a result, the divergence of the Pomeranchuk susceptibility is cut and this channel no longer competes with SC/SDW. Also, because the SC and the SDW channels do not mix below E_F , each develops independently in a mean-field fashion with the couplings taken at $L = L_F$ (Ref [5, 33]). If L_F is small enough, these values are close to the bare ones and the system develops SDW order (and Ising-nematic order above it, if SDW order is a stripe). When doping gets larger (and nesting gets weaker), SDW channel becomes less singular and SC order develops first. This behavior is consistent with the one observed in most FeSCs, for which the largest $E_F \sim 100$ meV well exceeds T_N , $T_c \sim 10$ meV (Ref. [49]). In FeSe, on the other hand, all $E_F \leq 10$ meV and are comparable to $T_s \sim 7$ meV [50].

Summary In this paper we employed the analytical pRG technique to analyze the interplay between SDW, SC, and orbital POM order in Fe-based superconducting materials. We computed the exponents for susceptibilities in SDW, SC, and POM channels and found that in FeSe, where all Fermi energies are small, the system develops a spontaneous ferro-orbital order, followed by s^{+-} superconductivity, while SDW order does not develop. In systems in which at least one of the pockets has E_F large, as in LaFeAsO, BaFe₂As₂, and NaFeAs, orbital order does not develop. Instead, SDW and SC orders compete with each other, with SC winning at higher doping and SDW winning at smaller doping. In this situation, nematic order is associated with stripe SDW. Our work provides an appealing unified microscopic description of the behavior of different families of FeSCs.

Acknowledgments We thank G. Blumberg, A. Boehmer, I. Fisher, P. Hirschfeld, C. Honerkamp, I. Eremin, S. Kivelson, H. Kontani, I. Mazin, C. Meingast, R. Thomale, V. K. Thorsmølle, O. Vafek, R. Valenti, and Y. Wang for useful discussions. This work was supported by the Office of Basic Energy Sciences, U.S. Department of Energy, under awards DE-FG02-ER46900 (AVC) and DE-SC0012336 (RMF). MK is supported by the Israel Science Foundation, Grant No. 1287/15 and NSF DMR-1506668.

-
- [1] Onari, S. and Kontani, H. Self-consistent vertex correction analysis for iron-based superconductors: Mechanism of Coulomb interaction-driven orbital fluctuations. Phys. Rev. Lett. 109, 137001 (2012); Yamakawa, Y., Onari, S., and Kontani, H. Nematicity and Magnetism in FeSe

- and other Families of Fe-based Superconductors. arXiv:1509.01161 (2015).
- [2] Mazin, I.I., Singh, D.J., Johannes, M.D., and Du, M.H. Unconventional Superconductivity with a Sign Reversal in the Order Parameter of $\text{LaFeAsO}_{1-x}\text{F}_x$. Phys. Rev. Lett. 101, 057003 (2008); Hirschfeld, P. J., Korshunov, M. M. and Mazin, I. I., Gap symmetry and structure of Fe-based superconductors. Rep. Prog. Phys. 74, 124508 (2011).
 - [3] Kuroki, K., Onari, S., Arita, R., Usui, H., Tanaka, Y., Kontani, H., and Aoki, H. Unconventional Pairing Originating from the Disconnected Fermi Surfaces of Superconducting $\text{LaFeAsO}_{1-x}\text{F}_x$. Phys. Rev. Lett. 101, 087004 (2008); Kuroki K., Usui, H., Onari, S., Arita, R., and Aoki, H. Pnictogen height as a possible switch between high-Tc nodeless and low-Tc nodal pairings in the iron-based superconductors. Phys. Rev. B 79, 224511 (2009).
 - [4] Kemper, A. F., Maier, T. A., Graser, S., Cheng, H.-P., Hirschfeld, P. J. and Scalapino, D. J. Sensitivity of the superconducting state and magnetic susceptibility to key aspects of electronic structure in ferropnictides. New Journal of Physics **12**, 073030 (2010); Graser, s., Maier, T. A., Hirschfeld, P. J. and Scalapino, D. J. Near-Degeneracy of Several Pairing Channels in Multiorbital Models for the Fe Pnictides. New Journal of Physics 11, 025016 (2009).
 - [5] Chubukov, A. V. Pairing mechanism in Fe-based superconductors. Annu. Rev. Condens. Matter Phys. 3, 57, (2012); Chubukov, A.V. Renormalization group analysis of competing orders and the pairing symmetry in Fe-based superconductors. Physica C **469**, 640 (2009).
 - [6] Yamase, H. and Zeyher, R. Superconductivity from orbital nematic fluctuations. Phys. Rev. B 88, 180502(R) (2013); Yamase, H and Zeyher, R. Spin nematic fluctuations near a spin-density-wave phase. New J. Phys. 17, 073030 (2015).
 - [7] Yin, Z. P., Haule, K., and Kotliar, G. Spin dynamics and an orbital-antiphase pairing symmetry in iron-based superconductors. Nature Phys. 10, 845 (2014).
 - [8] Dumitrescu, P. T., Serbyn, M., Scalettar, R. T., and Vishwanath, A Superconductivity and Nematic Fluctuations in a model of FeSe monolayers: A Determinant Quantum Monte Carlo Study. arXiv:1512:08523 (2015).
 - [9] Fernandes, R. M. Chubukov, A. V. and Schmalian, J. What drives nematic order in Fe-based superconductors? Nature Phys. 10, 97 (2014).
 - [10] Dai, P., Hu, J. and Dagotto, E. Magnetism and its microscopic origin in iron-based high-temperature superconductors. Nature Phys. 8, 7 (2012).
 - [11] Lee, C. C., Yin, W. G. and Ku, W. Ferro-orbital order and strong magnetic anisotropy in the

- parent compounds of iron-pnictide superconductors. Phys. Rev. Lett. 103, 267001 (2009).
- [12] Kruger, F. S., Kumar, J., Zaanen, J. and van den Brink, Spin-orbital frustrations and anomalous metallic state in iron-pnictide superconductors. Phys. Rev. B 79, 054504 (2009).
 - [13] Valenzuela, B., Bascones, E. and Calderon, M. J. Conductivity anisotropy in the antiferromagnetic state of iron pnictides. Phys. Rev. Lett. 105, 207202 (2010).
 - [14] Lv, W. and Phillips, P. Orbital and magnetically induced anisotropy in iron-based superconductors. Phys. Rev. B 84, 174512 (2011); Lee, W-C. and Phillips, P. W. Non-Fermi liquid due to orbital fluctuations in iron pnictide superconductors. Phys. Rev. B 86, 245113 (2012).
 - [15] Applegate, R., Singh, R. R. P., Chen, C-C. and Devereaux, T. P. Phase transitions in spin-orbital models with spin-space anisotropies for iron pnictides: Monte Carlo simulations. Phys. Rev. B 85, 054411 (2012).
 - [16] Brydon, P. M. R., Schmiedt, J., and Timm, C. Microscopically derived Ginzburg-Landau theory for magnetic order in the iron pnictides. Phys. Rev. B 84, 214510 (2011).
 - [17] Fernandes, R. M., Chubukov, A. V., Knolle, J., Eremin, I. and Schmalian, J. Preemptive Nematic order pseudogap, and orbital order in the iron pnictides. Phys. Rev. B 85, 024534 (2012).
 - [18] Stanev, V. and Littlewood, P. B. Nematicity driven by hybridization in iron-based superconductors. Phys. Rev. B 87, 161122(R) (2013).
 - [19] Liang, S., Moreo, A. and Dagotto, E. Nematic state of pnictides stabilized by interplay between spin, orbital, and lattice degrees of freedom. Phys. Rev. Lett. 111, 047004 (2013).
 - [20] Gastiasoro, M. N., and Andersen, B. M. Competing magnetic double-Q phases and superconductivity-induced reentrance of C_2 magnetic stripe order in iron pnictides. Phys. Rev. B 92, 140506(R) (2015).
 - [21] Chubukov, A.V., Fernandes, R. M. and Schmalian, J. The origin of nematic order in FeSe, Phys. Rev. B 91, 201105 (2015).
 - [22] Hinojosa, A., Cai, J. and Chubukov, A.V. Raman resonance in iron-based superconductors: The magnetic scenario. Phys. Rev. B 93, 075106 (2016).
 - [23] Baek, S.-H., Efremov, D. V., Ok, J. M., Kim, J. S., van den Brink, J. and Buchner, B. Orbital-driven nematicity in FeSe. Nat Mater 14, 210 (2015).
 - [24] Gallais, I. and Paul, I. Charge Nematicity and Electronic Raman Scattering in Iron-based Superconductors Comptes Rendus Physique 17, 113-139 (2016) and references therein;

- Thorsmølle, V.K., Khodas, M., Yin, Z. P., Zhang, Ch., Carr, S. V. , Dai, P. and Blumberg, G. Critical quadrupole fluctuations and collective modes in iron pnictide superconductors. Phys. Rev. B 93, 054515 (2016).
- [25] S. Lederer, Y. Schattner, E. Berg, and S. A. Kivelson, Phys. Rev. Lett. 114, 097001 (2015).
- [26] Fang, C., Yao, H., Tsai, W-F., Hu, J. and Kivelson, S. A. Theory of electron nematic order in LaFeAsO. Phys. Rev. B 77, 224509 (2008); Xu, C., Muller, M., and Sachdev, S. Ising and spin orders in the iron-based superconductors. Phys. Rev. B 78, 020501(R) (2008); Chandra, P., Coleman, P., and Larkin, A. I. Ising transition in frustrated Heisenberg models. Phys. Rev. Lett. 64, 88, (1990); Eremin, I. and Chubukov, A. V. Magnetic degeneracy and hidden metallicity of the spin-density-wave state in ferropnictides. Phys. Rev. B 81, 024511 (2010).
- [27] Fernandes, R.M. and Schmalian, J. Manifestations of nematic degrees of freedom in the magnetic, elastic, and superconducting properties of the iron pnictides. Supercond. Science and Technology 25, 084005 (2012).
- [28] Khodas, M. and Chubukov, A. V. Interpocket Pairing and Gap Symmetry in Fe-Based Superconductors with Only Electron Pockets. Phys. Rev. Lett. 108, 247003 (2012).
- [29] Kutepov, A., Haule, K., Savrasov, S. Y. and Kotliar, G. Self consistent GW determination of the interaction strength: application to the iron arsenide superconductors. Phys. Rev. B 82, 045105 (2010).
- [30] Fanfarillo, L., Cortijo, A., and Valenzuela, B. Spin-orbital interplay and topology in the nematic phase of iron pnictides. Phys. Rev. B 91, 214515 (2015).
- [31] Christensen, M. H., Kang, J., Andersen, B. M., Eremin, I., and and Fernandes, R. M. Spin reorientation driven by the interplay between spin-orbit coupling and Hund's rule coupling in iron pnictides. Phys. Rev. B 92, 214509 (2015).
- [32] Chubukov, A. V., Efremov, D. V. and Eremin, I. Magnetism, superconductivity, and pairing symmetry in iron-based superconductors. Phys. Rev. B 78, 134512 (2008).
- [33] Maiti, S and Chubukov, A. V. Renormalization group flow, competing phases, and the structure of superconducting gap in multiband models of iron-based superconductors. Phys. Rev. B **82**, 214515 (2010).
- [34] Yin, Z. P. , Haule, K. and Kotliar, G. Kinetic frustration and the nature of the magnetic and paramagnetic states in iron pnictides and iron chalcogenides. Nature Mater. 10, 932 (2011).
- [35] de' Medici, L. , Giovannetti, G. and Capone, M. Selective Mott Physics as a Key to Iron

- Superconductors. Phys. Rev. Lett. 112, 177001 (2014).
- [36] LeHur, K. and Rice, T. M. Superconductivity close to the Mott state: From condensed-matter systems to superfluidity in optical lattices. Ann. Phys. 324, 1452 (2009).
 - [37] Platt, C., Honerkamp, C., and Hanke, W. Pairing in the iron arsenides: a functional RG treatment. New J. Phys. 11, 055058 (2009)
 - [38] Platt, C., Hanke, W. and Thomale, R. Functional renormalization group for multi-orbital Fermi surface instabilities. Advances in Physics 62, 453-562 (2013).
 - [39] Yang, F., Wang, F., and Lee, D.-H. Fermiology, orbital order, orbital fluctuations, and Cooper pairing in iron-based superconductors. Phys. Rev. B 88, 100504 (2013).
 - [40] see e.g., Okazaki, K. et al., Octet-Line Node Structure of Superconducting Order Parameter in KFe_2As_2 . Science 337, 1314 (2012).
 - [41] Cvetkovic, V. and Vafeek, O. Space group symmetry, spin-orbit coupling and the low energy effective Hamiltonian for iron based superconductors. Phys. Rev. B 88, 134510 (2013); Cvetkovic, V. and Tesanovic, Z. Valley density-wave and multiband superconductivity in iron-based pnictide superconductors. Phys. Rev. B 80, 024512 (2009); Fernandes, R. M. and Vafeek, O. Distinguishing spin-orbit coupling and nematic order in the electronic spectrum of iron-based superconductors. Phys. Rev. B 90, 214514 (2014).
 - [42] When electron pockets are approximated as pure d_{xy} , some of u_i and \bar{u}_i turn out to be equal already at a bare level, see SM.
 - [43] and Di Castro, C. Fermi systems with strong forward scattering. Adv. Phys. 47, 317 (1998); M. Salmhofer, Continuous renormalization for fermions and Fermi liquid theory. Commun. Math. Phys. 194, 249 (1998).
 - [44] Murray, J. M., and Vafeek, O. Renormalization group study of interaction-driven quantum anomalous Hall and quantum spin Hall phases in quadratic band crossing systems, Phys. Rev. B 89, 201110(R) (2014)
 - [45] Nandkishore, L., Levitov, L., and Chubukov, A.V., Chiral superconductivity from repulsive interactions in doped graphene Nature Phys. 8, 158 (2012)
 - [46] Kiesel, M., Platt, C. Hanke, W., Abanin, D.A., and Thomale R., Competing many-body instabilities and unconventional superconductivity in graphene, Phys. Rev. B 86, 020507 (2012).
 - [47] Ortenzi, L., Cappelluti, E., Benfatto, I. and Pietronero, L. Fermi-Surface Shrinking and Interband Coupling in Iron-Based Pnictides, Phys. Rev. Lett. 103, 046404 (2009).

- [48] Dhaka, R. S., Hahn, S. E., Razzoli, E., Jiang, R., Shi, M., Harmon, B. N., Thaler, A., Bud'ko, S. L., Canfield, P. C., and Kaminski, A. Unusual Temperature Dependence of Band Dispersion in $\text{Ba}(\text{Fe}_{1-x}\text{Ru}_x)_2\text{As}_2$ and its Consequences for Antiferromagnetic Ordering. *Phys. Rev. Lett.* 110, 067002 (2013); Brouet, V. *et al*, Large Temperature Dependence of the Number of Carriers in Co-Doped BaFe_2As_2 . *Phys. Rev. Lett.* 110, 167002 (2013).
- [49] Johnston, D. C. The puzzle of high temperature superconductivity in layered iron pnictides and chalcogenides. *Adv. Phys.* 59, 803 (2010).
- [50] Watson, M. D., *et al* Emergence of the nematic electronic state in FeSe. *Phys. Rev. B* 91, 155106 (2015); Terashima, T. *et al* Anomalous Fermi surface in FeSe seen by Shubnikov-de Haas oscillation measurements. *Phys. Rev. B* 90, 144517 (2014); Charnukha, A. *et al* Weak-coupling superconductivity in a strongly correlated iron pnictide, *Sci. Rep.* 5, 18620 (2015) and references therein

SDW	CDW-r	CDW-i
$u_1 + u_3/C$	$u_1 - u_3/C - 2u_2$	$u_1 - 2u_2 + u_3/C$
SC s^{+-}	POM s	POM d
$2(-u_4 + u_3)$	$2(-u_4 + 4Cu_1)$	$-2u_4$

TABLE I: The interactions in different channels along the stable fixed trajectory. All interactions scale as $1/(L_0 - L)$ and diverge at RG scale L_0 . We use these interactions to compute vertices and susceptibilities in SDW channel, CDW channels with real and imaginary order parameters (CDW-r and CDW-i), s^{+-} superconducting channel, and s -wave and d -wave Pomeranchuk channels (POM s and POM d).

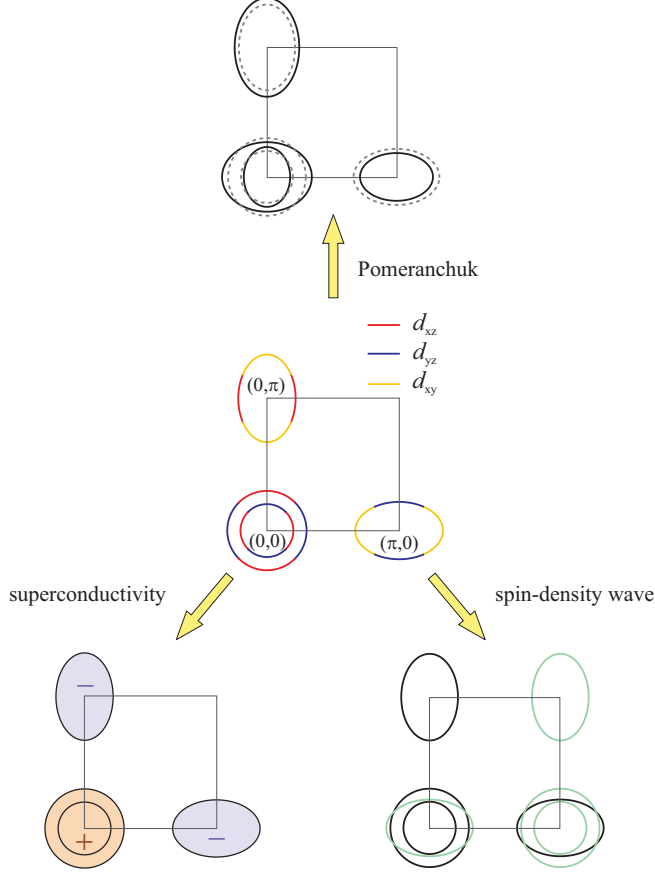


FIG. 1: Low-energy states and potential instabilities. The orbital content of the 2D Fermi surface of the Fe-based superconductors is plotted together with the changes in the fermionic excitations promoted by one of three electronic instabilities – s^{+-} superconductivity, stripe SDW magnetism, and nematicity (breaking of C_4 lattice rotational symmetry), which necessary gives rise to orbital order. The low-energy excitations live near hole-pockets centered at the Γ point ($k_x = k_y = 0$), and near electron pockets centered at $(0, \pi)$ ($\pi, 0$) in 1Fe Brillouin zone. Excitations near the hole pockets are made out of d_{xz} and d_{yz} orbitals, while the ones near the electron pockets are made out of d_{xz} and d_{xy} (d_{yz} and d_{xy}) orbitals. (Refs.[3, 4]). In some systems, there exists a third hole pocket (not shown) centered at (π, π) and made out of the d_{xy} orbital. s^{+-} superconductivity gaps out low-energy excitations, and the superconducting order parameter changes sign between hole and electron pockets. Stripe SDW magnetism with momentum $(0, \pi)$ or $(\pi, 0)$ (shown) mixes hole and electron states by band-folding and split hole and electron pockets into even smaller sub-pockets. Orbital order elongates the two hole pockets in opposite directions and makes one electron pocket larger and the other one smaller.

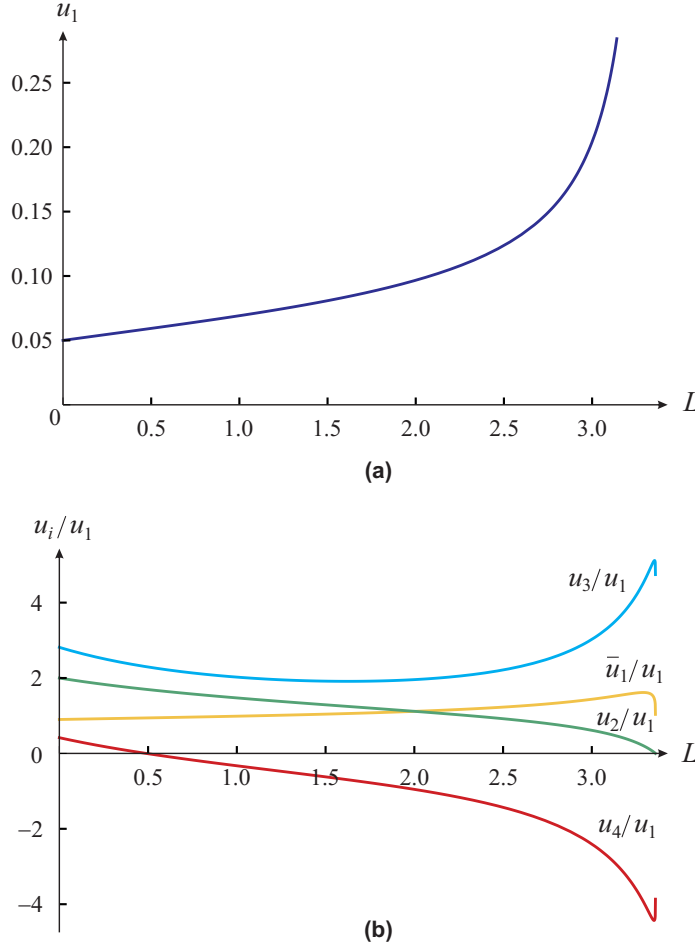


FIG. 2: **The pRG flow of the couplings.** Panel (a) – $u_1(L)$, where $L = \log W/E$ is the RG scale, W is the bandwidth, and E is the running energy (temperature) at which one probes the system. The flow of other couplings is similar. The couplings $u_1 - u_5$ and $\bar{u}_1 - \bar{u}_5$ all diverge as $1/(L_0 - L)$ when L approaches L_0 , whose value depends on the initial conditions. The couplings $\tilde{u}_4, \tilde{\bar{u}}_4, \tilde{u}_5, \tilde{\bar{u}}_5$ tend to zero at $L \rightarrow L_0$. Panel (b) – flow of the ratios of the couplings. All ratios tend to fixed finite values as L approaches L_0 : $\bar{u}_1 = u_1$, $u_3 = \bar{u}_3 = 4.7u_1$, $u_4 = u_5 = \bar{u}_4 = \bar{u}_5 = -3.8u_1$ (see Eq. 4). The ratios u_2/u_1 and \bar{u}_2/u_1 tend to zero as L approaches L_0 . The initial values used were $\bar{u}_1/u_1 = 0.9$, $u_2/u_1 = 2$, $u_3/u_1 = 2.8$, $u_4/u_1 = 0.4$. In both panels we set $C = (m_e + m_h)/(2\sqrt{m_e m_h}) = 1.1$ for definiteness. For the model with electron pockets the fixed trajectory is the same, but the system approaches it much faster (see SM).

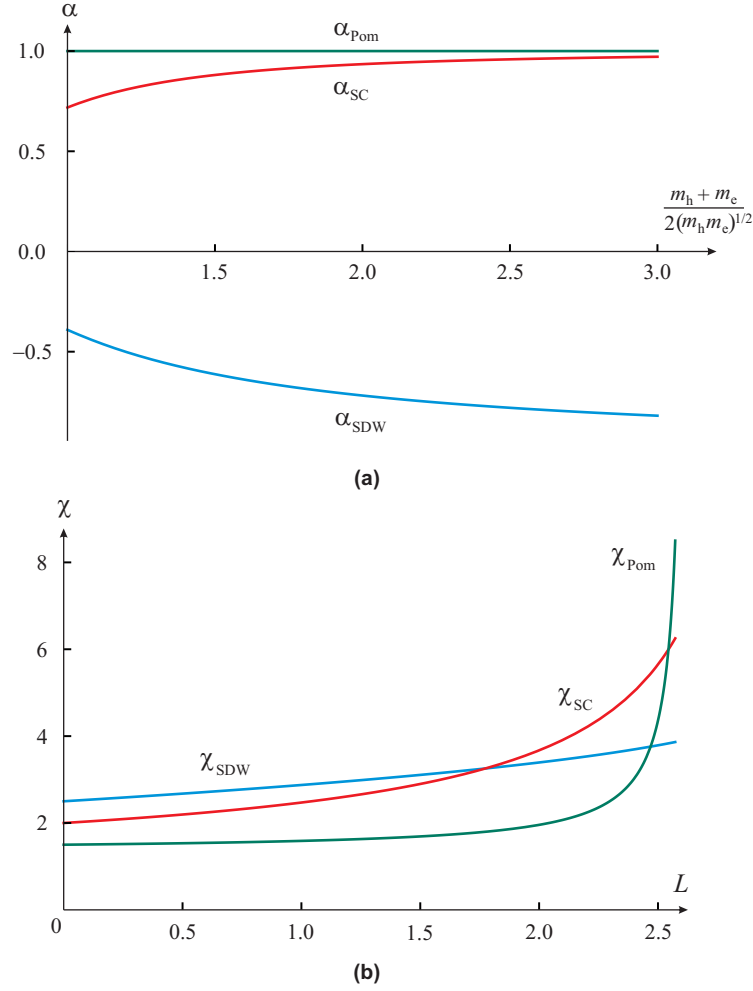


FIG. 3: **The pRG flow of the susceptibilities.** (a) The exponents for the susceptibilities $\chi_i \propto 1/(L_0 - L)_i^\alpha$ in SDW, s^{+-} SC, and POM channels as functions of $C = (m_e + m_h)/(2\sqrt{m_e m_h})$. The largest exponent $\alpha_{\text{POM}} = 1$ is in the Pomeranchuk channel. The exponent $\alpha_{\text{SDW}} < 0$, what implies that within pRG χ_{SDW} does not diverge. (b) The behavior of susceptibilities in SDW, s^{+-} SC, and POM channels. The Pomeranchuk susceptibility actually diverges at $L = L_P < L_0$. As a result, the leading instability upon lowering the temperature is towards d-wave orbital ordering. s^{+-} superconductivity develops at a smaller T , and SDW instability does not develop. This holds when L_0 is smaller than $L_F = \log W/E_F$, i.e., if the instability develops at an energy/temperature larger than E_F . If $L_F < L_0$, the pRG flow runs up to $L = L_F$, and at larger L SDW and SC channel decouple and develop independent on each other, while the Pomeranchuk channel gets frozen. In this situation, the system first develops either SDW or SC order, depending on the interplay between L_F and L_0 and the degree of nesting.

Supplementary material for “Magnetism, superconductivity, and spontaneous orbital order in iron-based superconductors: who comes first and why?”

I. MODEL HAMILTONIAN

We follow Ref. [41] to construct the low energy Hamiltonian. We introduce low-energy spinor wave function $\psi_\sigma^\dagger(\mathbf{q}) = [f_{1,\sigma}^\dagger(\mathbf{q}), f_{2,\sigma}^\dagger(\mathbf{q}), d_{1,\sigma}^\dagger(\mathbf{q}), d_{2,\sigma}^\dagger(\mathbf{q})]$, where the subscripts $\mu, \nu = 1, 2$ refer to the xz and yz orbital content respectively. Below we use 1-Fe Brillouin zone and neglect processes with momentum transfer (π, π) , which may be present due to the difference between the hopping via pnictogen/chalcogen atoms above and below the iron layer.

A. Transformation from the orbital to the band basis

The quadratic part of the Hamiltonian is expressed in terms of the components of the spinor $\psi_\sigma^\dagger(\mathbf{q})$ as follows,

$$\mathcal{H}_0 = \sum_{\mathbf{k}, \alpha} \sum_{\mu, \nu=1,2} d_{\mu,\alpha}^\dagger(\mathbf{k}) \mathcal{H}_{\mu,\nu}^\Gamma(\mathbf{k}) d_{\nu,\alpha}(\mathbf{k}) + f_{\mu\alpha}^\dagger(\mathbf{k}) \mathcal{H}_{\mu,\nu}^M(\mathbf{k}) f_{\nu,\alpha}(\mathbf{k}), \quad (10)$$

The effective Hamiltonian is specified by

$$\mathcal{H}^\Gamma(\mathbf{k}) = \begin{bmatrix} \epsilon_\Gamma + \frac{k^2}{2m_\Gamma} + ak^2 \cos 2\theta_k & ck^2 \sin 2\theta_k \\ ck^2 \sin 2\theta_k & \epsilon_\Gamma + \frac{k^2}{2m_\Gamma} - ak^2 \cos 2\theta_k \end{bmatrix} \quad (11)$$

for holes, and by

$$\mathcal{H}^M(\mathbf{k}) = \begin{bmatrix} \epsilon_M + \frac{k^2}{2m_M} + bk^2 \cos 2\theta_k & 0 \\ 0 & \epsilon_M + \frac{k^2}{2m_M} - bk^2 \cos 2\theta_k \end{bmatrix} \quad (12)$$

for electrons. In Eqs. (11) and (12) we denote $\theta_k = \arctan(k_y/k_x)$, $\epsilon_{\Gamma,M}$, $1/m_{\Gamma,M}$, a , b and c are parameters of the model which are determined by the band structure calculations. In our approximation the electron’s Hamiltonian, (12) is diagonal and $f_{1,2}$ are the actual electron band operators. To simplify calculations, we set $a = c$ in (11) in which case the

two hole FSs are circular. The transformation from orbital to band basis in Eq. (11) is just a rotation

$$\begin{aligned} d_{1k\sigma} &= c_{k\sigma} \cos \theta_{k\sigma} + d_{k\sigma} \sin \theta_{k\sigma} \\ d_{2k\sigma} &= -c_{k\sigma} \sin \theta_{k\sigma} + d_{k\sigma} \cos \theta_{k\sigma}. \end{aligned} \quad (13)$$

For $a \neq c$ the transformation to the band basis remains the same as Eq. (13), with the rotation angle $\tilde{\theta}$ that is not identical to the angle θ formed by the vector \mathbf{k} with a given axis. In terms of the band operators, the kinetic energy, Eq. (10) is diagonal,

$$\mathcal{H}_0 = \sum_{\mathbf{k}, \alpha} \left[\epsilon_c(\mathbf{k}) c_{k\sigma}^\dagger c_{k\sigma} + \epsilon_d(\mathbf{k}) d_{k\sigma}^\dagger d_{k\sigma} + \epsilon_1(\mathbf{k}) f_{1,k\sigma}^\dagger f_{1,k\sigma} + \epsilon_2(\mathbf{k}) f_{2,k\sigma}^\dagger f_{2,k\sigma} \right], \quad (14)$$

where we absorbed the constant terms into the chemical potential. The band dispersions are

$$\epsilon_{c,d} = -\frac{k^2}{2m_{c,d}}, \quad \epsilon_{1,2}(\mathbf{k}) = \frac{k_x^2}{2m_{x,y}} + \frac{k_y^2}{2m_{x,y}}. \quad (15)$$

$$m_{c,d}^{-1} = m_\Gamma^{-1} \pm 2a, \text{ and } m_{x,y}^{-1} = m_M^{-1} \pm 2b.$$

B. Interaction Hamiltonian

We depart from the local Hubbard-Hund interaction, in the notations of Ref. [4]

$$H_i = U \sum_{i,\mu} n_{i,\mu\uparrow} n_{i,\mu\downarrow} + U' \sum_{i,\mu < \mu'} n_{i\mu} n_{i\mu'} + J \sum_{i,\mu' < \mu} \sum_{\sigma\sigma'} \psi_{i\mu\sigma}^\dagger \psi_{i\mu'\sigma'}^\dagger \psi_{i\mu\sigma} \psi_{i\mu'\sigma'} + J' \sum_{i,\mu' \neq \mu} \psi_{i\mu\uparrow}^\dagger \psi_{i\mu\downarrow}^\dagger \psi_{i\mu'\downarrow} \psi_{i\mu'\uparrow}, \quad (16)$$

where the index i enumerates the iron sites located at \mathbf{R}_i and

$$\psi_{\mu\sigma}(\mathbf{R}_j) = \frac{1}{\sqrt{N}} \sum_{\mathbf{q}} \left[d_{\mu\sigma}(\mathbf{k}) + f_{\mu\sigma}(\mathbf{k}) e^{i\mathbf{Q}_{1(2)} \cdot \mathbf{R}_j} \right] e^{i\mathbf{k} \cdot \mathbf{R}_j} \quad (17)$$

is the annihilation operator of an electron at the iron site located at \mathbf{R}_j with spin σ in the orbital state labeled by μ ($\mu = 1$ and $\mu = 2$ refer to xz and yz orbitals respectively). Further, $n_{i\mu\sigma} = \psi_{i\mu\sigma}^\dagger \psi_{i\mu\sigma}$ is the density operator, $n_{i\mu} = n_{i\mu\uparrow} + n_{i\mu\downarrow}$, and N is the number of iron atoms. The Eq. (16) can be rewritten in an SU(2) invariant form as

$$H_i = \frac{U}{2} \sum_{i,\mu} n_{i,\mu} n_{i,\mu} + \frac{U'}{2} \sum_{i,\mu \neq \mu'} n_{i\mu} n_{i\mu'} + \frac{J}{2} \sum_{i,\mu' \neq \mu} \sum_{\sigma\sigma'} \psi_{i\mu\sigma}^\dagger \psi_{i\mu'\sigma'}^\dagger \psi_{i\mu\sigma} \psi_{i\mu'\sigma'} + \frac{J'}{2} \sum_{i,\mu' \neq \mu} \psi_{i\mu\sigma}^\dagger \psi_{i\mu\sigma'}^\dagger \psi_{i\mu'\sigma'} \psi_{i\mu'\sigma}. \quad (18)$$

Substituting Eq. (17) into Eq. (18) we obtain

$$\begin{aligned}
H_{UJ} = & \frac{U}{2} \sum' \left[(f_{1\sigma}^\dagger f_{1\sigma} + d_{1\sigma}^\dagger d_{1\sigma})^2 + (f_{2\sigma}^\dagger f_{2\sigma} + d_{2\sigma}^\dagger d_{2\sigma})^2 + (f_{1\sigma}^\dagger d_{1\sigma} + d_{1\sigma}^\dagger f_{1\sigma})^2 + (f_{2\sigma}^\dagger d_{2\sigma} + d_{2\sigma}^\dagger f_{2\sigma})^2 \right] \\
& + U' \sum' (f_{1\sigma}^\dagger f_{1\sigma} + d_{1\sigma}^\dagger d_{1\sigma})(f_{2\sigma'}^\dagger f_{2\sigma'} + d_{2\sigma'}^\dagger d_{2\sigma'}) \\
& + J \sum' (f_{1\sigma}^\dagger f_{2\sigma} f_{2\sigma'}^\dagger f_{1\sigma'} + d_{1\sigma}^\dagger d_{2\sigma} d_{2\sigma'}^\dagger d_{1\sigma'} + f_{1\sigma}^\dagger d_{2\sigma} d_{2\sigma'}^\dagger f_{1\sigma'} + d_{1\sigma}^\dagger f_{2\sigma} f_{2\sigma'}^\dagger d_{1\sigma'}) \\
& + \frac{J'}{2} \sum' (f_{1\sigma}^\dagger f_{2\sigma} f_{1\sigma'}^\dagger f_{2\sigma'} + d_{1\sigma}^\dagger d_{2\sigma} d_{1\sigma'}^\dagger d_{2\sigma'} + f_{1\sigma}^\dagger d_{2\sigma} f_{1\sigma'}^\dagger d_{2\sigma'} + d_{1\sigma}^\dagger f_{2\sigma} d_{1\sigma'}^\dagger f_{2\sigma'} + h.c.)
\end{aligned} \tag{19}$$

Here the momenta arguments of the fermion operators in each term, $\mathbf{k}_1, \mathbf{k}_2, \mathbf{k}_3, \mathbf{k}_4$ are omitted for clarity, and \sum' stands for the summation over the spin indices, σ, σ' and over fermion momenta subject to $\mathbf{k}_1 - \mathbf{k}_2 + \mathbf{k}_3 - \mathbf{k}_4 = 0$, and also includes the normalization factor $1/N$.

The initial observation, which sets the stage for the RG analysis is that Eq. (19) is not the most general one consistent with the tetragonal symmetry. The most general interaction has the form

$$\begin{aligned}
H = & U_1 \sum' \left[f_{1\sigma}^\dagger f_{1\sigma} d_{1\sigma'}^\dagger d_{1\sigma'} + f_{2\sigma}^\dagger f_{2\sigma} d_{2\sigma'}^\dagger d_{2\sigma'} \right] + \bar{U}_1 \sum' \left[f_{2\sigma}^\dagger f_{2\sigma} d_{1\sigma'}^\dagger d_{1\sigma'} + f_{1\sigma}^\dagger f_{1\sigma} d_{2\sigma'}^\dagger d_{2\sigma'} \right] \\
& + U_2 \sum' \left[f_{1\sigma}^\dagger d_{1\sigma} d_{1\sigma'}^\dagger f_{1\sigma'} + f_{2\sigma}^\dagger d_{2\sigma} d_{2\sigma'}^\dagger f_{2\sigma'} \right] + \bar{U}_2 \sum' \left[f_{1\sigma}^\dagger d_{2\sigma} d_{2\sigma'}^\dagger f_{1\sigma'} + f_{2\sigma}^\dagger d_{1\sigma} d_{1\sigma'}^\dagger f_{2\sigma'} \right] \\
& + \frac{U_3}{2} \sum' \left[f_{1\sigma}^\dagger d_{1\sigma} f_{1\sigma'}^\dagger d_{1\sigma'} + f_{2\sigma}^\dagger d_{2\sigma} f_{2\sigma'}^\dagger d_{2\sigma'} + h.c. \right] + \frac{\bar{U}_3}{2} \sum' \left[f_{1\sigma}^\dagger d_{2\sigma} f_{1\sigma'}^\dagger d_{2\sigma'} + f_{2\sigma}^\dagger d_{1\sigma} f_{2\sigma'}^\dagger d_{1\sigma'} + h.c. \right] \\
& + \frac{U_4}{2} \sum' \left[d_{1\sigma}^\dagger d_{1\sigma} d_{1\sigma'}^\dagger d_{1\sigma'} + d_{2\sigma}^\dagger d_{2\sigma} d_{2\sigma'}^\dagger d_{2\sigma'} \right] + \frac{\bar{U}_4}{2} \sum' \left[d_{1\sigma}^\dagger d_{2\sigma} d_{1\sigma'}^\dagger d_{2\sigma'} + d_{2\sigma}^\dagger d_{1\sigma} d_{2\sigma'}^\dagger d_{1\sigma'} \right] \\
& + \tilde{U}_4 \sum' d_{1\sigma}^\dagger d_{1\sigma} d_{2\sigma'}^\dagger d_{2\sigma'} + \tilde{\bar{U}}_4 \sum' d_{1\sigma}^\dagger d_{2\sigma} d_{2\sigma'}^\dagger d_{1\sigma'} \\
& + \frac{U_5}{2} \sum' \left[f_{1\sigma}^\dagger f_{1\sigma} f_{1\sigma'}^\dagger f_{1\sigma'} + f_{2\sigma}^\dagger f_{2\sigma} f_{2\sigma'}^\dagger f_{2\sigma'} \right] + \frac{\bar{U}_5}{2} \sum' \left[f_{1\sigma}^\dagger f_{2\sigma} f_{1\sigma'}^\dagger f_{2\sigma'} + f_{2\sigma}^\dagger f_{1\sigma} f_{2\sigma'}^\dagger f_{1\sigma'} \right] \\
& + \tilde{U}_5 \sum' f_{1\sigma}^\dagger f_{1\sigma} f_{2\sigma'}^\dagger f_{2\sigma'} + \tilde{\bar{U}}_5 \sum' f_{1\sigma}^\dagger f_{2\sigma} f_{2\sigma'}^\dagger f_{1\sigma'} .
\end{aligned} \tag{20}$$

One can verify that each term in Eq. (20) obeys the tetragonal symmetry separately. Eq. (20) contains 14 independent coupling constants. We split these 14 couplings into a three subsets that are not mixed with each other under the pRG flow. These three subsets are presented graphically in Figs. 4, 5 and 6.

We show below that the amplitudes from different subsets do not mix under the pRG flow. The full three-orbital model, which includes d_{xy} components on electron pockets, contains 30 independent coupling constants [41]. The comparison between Eqs. (19) and (20)

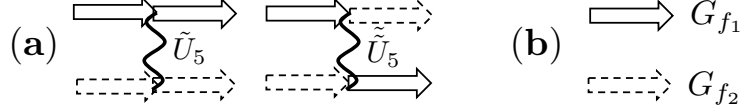


FIG. 4: (a) The subset of the interactions defined by Eq. (20). (b) The graphical representation of the electron propagators, introduced in Eq. (26).

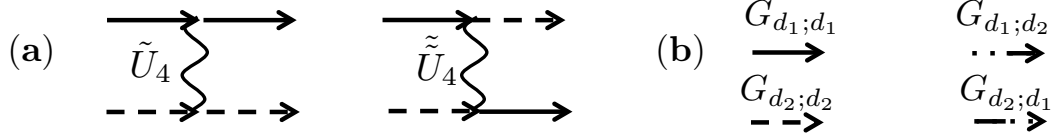


FIG. 5: (a) The subset of the interactions defined by Eq. (20). (b) The graphical representation of the hole propagators in the orbital representation, introduced in Eqs. (35) and (36).

gives the following relations,

$$\begin{aligned}
 U_1 &= U_2 = U_3 = U_4 = U_5 = U, \\
 \bar{U}_1 &= \tilde{U}_4 = \tilde{U}_5 = U', \\
 \bar{U}_2 &= \tilde{U}_4 = \tilde{U}_5 = J, \\
 \bar{U}_3 &= \bar{U}_4 = \bar{U}_5 = J'.
 \end{aligned} \tag{21}$$

These relations hold for bare couplings, but, as we will see, are not preserved under the pRG flow. On the other hand RG flow does not generate new couplings in addition to 14 in Eq. (20), i.e., the model with 14 coupling is renormalizable.

The splitting between different couplings in Eq. (21) implies that RG flow generates non-local interactions. The information extracted from the low-energy sector only is not sufficient to fully specify which non-local interactions are generated, but the model with 14 couplings can be constructed if one adds to local U, U', J, J' also interactions of the same Hubbard and Hund type, but involving fermions from different sites of each plaquette on a square lattice. Thus 5 terms involving fermions from the same orbital d_{xz} or d_{yz} (U_1, U_2, U_3, U_4 , and U_5 terms) appear with different couplings if we introduce, in addition to on-site

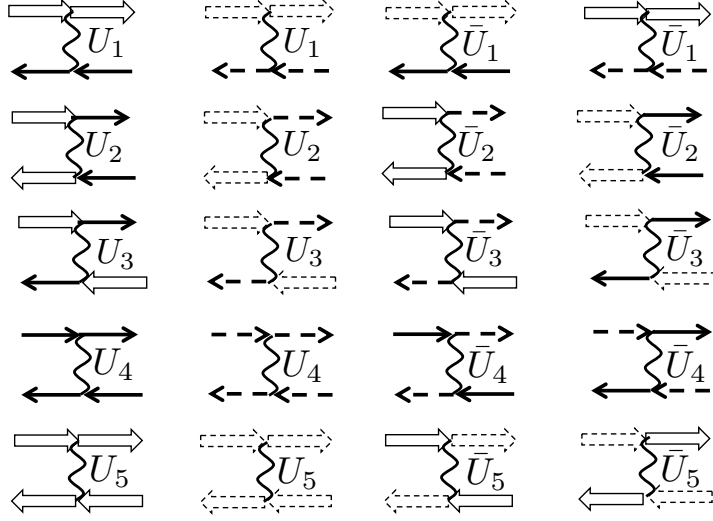


FIG. 6: The subset of the interactions defined by Eq. (20).

U , also the terms

$$\begin{aligned}
\mathcal{H}_{non-local} = & \sum_r U_a d_{xz}^\dagger(r) d_{xz}(r) d_{xz}^\dagger(r + a_y) d_{xz}(r + a_y) + U_b d_{xz}^\dagger(r) d_{xz}(r) d_{xz}^\dagger(r + a_x) d_{xz}(r + a_x) \\
& + U_c d_{xz}^\dagger(r) d_{xz}(r + a_y) d_{xz}^\dagger(r + a_x) d_{xz}(r + a_x + a_y) \\
& + U_d d_{xz}^\dagger(r) d_{xz}(r + a_x) d_{xz}^\dagger(r + a_y) d_{xz}(r + a_x + a_y) + h.c
\end{aligned} \tag{22}$$

and analogous (symmetry-related terms) for d_{yz} orbital. In (22) a_x and a_y are the components of the lattice spacing \mathbf{a} . The couplings U_i ($i = 1 - 5$) are now given by

$$\begin{aligned}
U_1 &= U + U_a - U_b - U_c - U_d, & U_2 &= U - U_a - U_b - U_c - U_d, & U_3 &= U - U_a + U_b + U_c - U_d, \\
U_4 &= U + U_a + U_b + U_c + U_d, & U_5 &= U + U_a - U_b + U_c + U_d
\end{aligned} \tag{23}$$

One can easily verify that the interactions within a given plaquette involving fermions from different orbitals splits U' , J , and J' terms into subsets each consisting of three different interactions (there are 5 terms in each subset, like in Eq. (22), but there are only three non-equivalent combinations of different U'_i , J_i and J'_i).

II. PRG EQUATIONS AND AMPLITUDES

We define the RG variable L at energy/temperature scale E as $L = \log \frac{W}{E}$, where W is of order bandwidth. The variable L increases starting from $L = 0$ at $E = W$.

The four-fermion interaction vertices in terms of band operators are obtained by using Eq. (13) and identifying $f_{1,2}$ with the corresponding band operators. Each vertex involves two creation and two annihilation fermionic operators either from one of two hole pockets (c_k and d_k) or from two electron pockets $f_{1,k}$ and $f_{2,k}$. The prefactors are the combinations of $\cos \theta_k$ and $\sin \theta_k$ from the transformation in Eq. (13). The total number of the interaction terms in the band basis is 152. We verified that demonstrate that all the terms within each of the 14 combinations in Eq. (20) flow identically under pRG. We show that the pRG equations split into three groups which remain separate under pRG flow. The first group includes interactions \tilde{U}_5 and $\tilde{\tilde{U}}_5$. The second group includes \tilde{U}_4 and $\tilde{\tilde{U}}_4$, and the third group contains ten remaining interactions: U_i , \bar{U}_i with $i = 1 - 5$. Below we analyse these three groups of pRG equations separately.

A. The pRG for the interactions \tilde{U}_5 and $\tilde{\tilde{U}}_5$

It is instructive to consider first the flow of \tilde{U}_5 and $\tilde{\tilde{U}}_5$ (see Fig. 4) because they describe interactions between fermions from the two electron pockets and get renormalized only in the particle-particle channel (see Fig. 7).

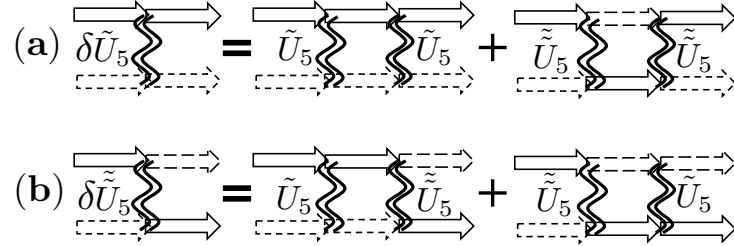


FIG. 7: Diagrammatic representation of the renormalizations of the interactions \tilde{U}_5 , (a) and $\tilde{\tilde{U}}_5$, (b), to second order in the interactions.

The corresponding terms in the four-fermion Hamiltonian(20) are

$$H_{\tilde{U}_5} + H_{\tilde{\tilde{U}}_5} = \tilde{U}_5 \sum_{\sigma\sigma'} \sum' [f_{1,\sigma,\mathbf{k}_1}^\dagger f_{2,\sigma',\mathbf{k}_3}^\dagger] [f_{2,\sigma',\mathbf{k}_4} f_{1,\sigma,\mathbf{k}_2}] + \tilde{\tilde{U}}_5 \sum_{\sigma\sigma'} \sum' [f_{1,\sigma,\mathbf{k}_1}^\dagger f_{2,\sigma',\mathbf{k}_3}^\dagger] [f_{1,\sigma',\mathbf{k}_4} f_{2,\sigma,\mathbf{k}_2}]. \quad (24)$$

The logarithmic renormalization in the particle-particle channel is obtained when either $\mathbf{k}_4 \approx -\mathbf{k}_2 \approx \mathbf{k}$ or $\mathbf{k}_1 \approx -\mathbf{k}_3 \approx \mathbf{k}$ in Eq. (24) are the running (larger) momentum, with no

kinematical constraints on external (small) momenta $\mathbf{k}_{1(4)}, \mathbf{k}_{3(2)}$, which we assume to be of the same order and label as k_{ext} .

Let the amplitudes at a running momentum k be $\tilde{U}_5(k)$ and $\tilde{\tilde{U}}_5(k)$. Using the standard reasoning for pRG, i.e., selecting the cross-section in the diagram in Fig. 7

with the smallest running momentum momentum k , integrating over larger momenta (in logarithmical sense) on both sides of this cross-section to get running $\tilde{U}_5(k)$ and $\tilde{\tilde{U}}_5(k)$, and integrating over k with k_{ext} as the lower limit, we obtain running couplings $\tilde{U}_5(k_{ext})$ and $\tilde{\tilde{U}}_5(k_{ext})$. The equation for $\tilde{U}_5(k_{ext})$, obtained this way, reads

$$\tilde{U}_5(k_{ext}) = - \int_{k_{ext}} \frac{d^2 \mathbf{k}}{4\pi^2} ((\tilde{U}_5(k))^2 + (\tilde{\tilde{U}}_5(k))^2) \int \frac{d\epsilon}{2\pi} G_{f_1}(i\epsilon, \mathbf{k}) G_{f_2}(-i\epsilon, -\mathbf{k}), \quad (25)$$

where

$$G_{f_{1,2}}(i\epsilon, k) = \frac{1}{i\epsilon - \epsilon_{1,2}(\mathbf{k}) - \mu} \quad (26)$$

are the Green functions for the xz and yz electrons with dispersions (15). The integration over frequency and over directions of \mathbf{k} yield

$$\begin{aligned} & \int \frac{d\phi}{2\pi} \int \frac{d\epsilon}{2\pi} G_{f_1}(i\epsilon, \epsilon_{f_1}(k)) G_{f_2}(-i\epsilon, \epsilon_{f_2}(-k)) = \int \frac{d\phi}{2\pi} \frac{1}{\xi_{f_1} + \xi_{f_2}} \\ &= \int \frac{d\phi}{2\pi} \frac{1}{\frac{k_x^2}{2m_x} + \frac{k_y^2}{2m_y} + \frac{k_x^2}{2m_y} + \frac{k_y^2}{2m_x}} \\ &= \frac{2m_x m_y}{m_x + m_y} \frac{1}{k^2}. \end{aligned} \quad (27)$$

Substituting this into (25) we obtain

$$\tilde{U}_5(k_{ext}) = - \frac{2m_x m_y}{m_x + m_y} \int_{k_{ext}} \frac{dk^2}{4\pi k^2} ((\tilde{U}_5(k))^2 + (\tilde{\tilde{U}}_5(k))^2). \quad (28)$$

Introducing the logarithmical variable $L = \log \frac{Wm}{k_{ext}^2}$ we obtain

$$4\pi \frac{d\tilde{U}_5(L)}{dL} = - \frac{2m_x m_y}{m_x + m_y} ((\tilde{U}_5(L))^2 + (\tilde{\tilde{U}}_5(L))^2). \quad (29)$$

Similarly,

$$4\pi \frac{d\tilde{\tilde{U}}_5}{dL} = -2 \frac{2m_x m_y}{m_x + m_y} \tilde{U}_5 \tilde{\tilde{U}}_5. \quad (30)$$

Introducing dimensionless interactions as

$$\tilde{u}_5 = \frac{2m_x m_y}{m_x + m_y} \frac{\tilde{U}_5}{4\pi}, \quad \tilde{\tilde{u}}_5 = \frac{2m_x m_y}{m_x + m_y} \frac{\tilde{\tilde{U}}_5}{4\pi} \quad (31)$$

we cast the pRG equations (29) and (30) in the following form,

$$\begin{aligned}\frac{d\tilde{u}_5}{dL} &= -(\tilde{u}_5^2 + \tilde{\tilde{u}}_5^2), \\ \frac{d\tilde{\tilde{u}}_5}{dL} &= -2\tilde{u}_5\tilde{\tilde{u}}_5.\end{aligned}\tag{32}$$

Eqs. (32) could be obtained also in the Wilsonian RG scheme, in which one *assumes* renormalizability (i.e. assumes that the couplings depend on the running rather than initial momenta) and integrates in (32) over momenta in the annulus $k - dk < k' < k$. In this procedure

$$\begin{aligned}d\tilde{U}_5(k) &= -((\tilde{U}_5(k))^2 + (\tilde{\tilde{U}}_5(k))^2) \int_{dk} \frac{d^2\mathbf{k}}{4\pi^2} \int \frac{d\epsilon}{2\pi} G_{f_1}(i\epsilon, \mathbf{k}) G_{f_2}(-i\epsilon, -\mathbf{k}) \\ &= -((\tilde{U}_5(k))^2 + (\tilde{\tilde{U}}_5(k))^2) \frac{2m_x m_y}{m_x + m_y} \frac{dL}{4\pi}.\end{aligned}\tag{33}$$

Differentiating over dL one obtains the same equation as (29). The Wilsonian RG scheme is more common and we will use it for the derivation of other RG equations.

It follows from the Eq. (32) that the pRG flow moves the repulsive interactions $\tilde{u}_5, \tilde{\tilde{u}}_5 > 0$ towards zero provided at the bare level (i.e. at energies comparable to Λ) $\tilde{u}_5 > \tilde{\tilde{u}}_5$. According according to Eq. (21) this holds when $U' > J$. As this condition is supposed to be satisfied, we may safely set \tilde{u}_5 and $\tilde{\tilde{u}}_5$ to zero.

We note in passing that the logarithmical renormalization in the particle-particle channel is not the Cooper effect because we integrate over momenta well above k_F . Rather it is related to the fact that in 2D and for k^2 dispersion of fermions, the scattering amplitude is logarithmically singular, what physically implies that even a weak attraction between two fermions gives rise to the development of a bound state.

B. The pRG for the interactions \tilde{U}_4 and $\tilde{\tilde{U}}_4$

The interactions \tilde{U}_4 and $\tilde{\tilde{U}}_4$ (see Fig. 5) are also renormalized only in the particle-particle channel. In this case, however the band basis differs from the orbital basis and the transformation (13) is required in order to find the right pRG equations.

In the orbital representation the change of \tilde{U}_4 and $\tilde{\tilde{U}}_4$ due to integration over the ring

$k - dk < k < k$ is

$$\begin{aligned}
d\tilde{U}_4 &= -(\tilde{U}_4^2 + \tilde{\tilde{U}}_4^2) \int_{dk} \frac{d^2 \mathbf{k}}{4\pi^2} \int \frac{d\epsilon}{2\pi} G_{d_1;d_1}(i\epsilon, \mathbf{k}) G_{d_2;d_2}(-i\epsilon, -\mathbf{k}) \\
&\quad - 2\tilde{U}_4 \tilde{\tilde{U}}_4 \int_{dk} \frac{d^2 \mathbf{k}}{4\pi^2} \int \frac{d\epsilon}{2\pi} G_{d_1;d_2}(i\epsilon, \mathbf{k}) G_{d_2;d_1}(-i\epsilon, -\mathbf{k}) \\
d\tilde{\tilde{U}}_4 &= -2\tilde{U}_4 \tilde{\tilde{U}}_4 \int_{dk} \frac{d^2 \mathbf{k}}{4\pi^2} \int \frac{d\epsilon}{2\pi} G_{d_1;d_1}(i\epsilon, \mathbf{k}) G_{d_2;d_2}(-i\epsilon, -\mathbf{k}) \\
&\quad - (\tilde{U}_4^2 + \tilde{\tilde{U}}_4^2) \int_{dk} \frac{d^2 \mathbf{k}}{4\pi^2} \int \frac{d\epsilon}{2\pi} G_{d_1;d_2}(i\epsilon, \mathbf{k}) G_{d_2;d_1}(-i\epsilon, -\mathbf{k}), \tag{34}
\end{aligned}$$

The Greens functions in the orbital representation, $G_{d_i;d_j}(i\epsilon, \mathbf{k})$ are expressed via the propagators of low-energy fermions in the band representation,

$$G_{c(d)}(i\epsilon, \mathbf{k}) = \frac{1}{i\epsilon - \epsilon_{c(d)}(\mathbf{k}) - \mu} \tag{35}$$

as

$$\begin{aligned}
G_{d_1,d_1}(i\epsilon, \mathbf{k}) &= G_c(i\epsilon, \mathbf{k}) \cos^2 \theta_{\mathbf{k}} + G_d(i\epsilon, \mathbf{k}) \sin^2 \theta_{\mathbf{k}}, \\
G_{d_2,d_2}(i\epsilon, \mathbf{k}) &= G_c(i\epsilon, \mathbf{k}) \sin^2 \theta_{\mathbf{k}} + G_d(i\epsilon, \mathbf{k}) \cos^2 \theta_{\mathbf{k}}, \\
G_{d_1,d_2}(i\epsilon, \mathbf{k}) &= G_{d_2,d_1}(i\epsilon, \mathbf{k}) = [G_d(i\epsilon, \mathbf{k}) - G_c(i\epsilon, \mathbf{k})] \sin \theta_{\mathbf{k}} \cos \theta_{\mathbf{k}}. \tag{36}
\end{aligned}$$

The band dispersions $\epsilon_{c(d)}(\mathbf{k})$ are given in Eq. (15). The Eq. (34) is illustrated in Fig. 8.

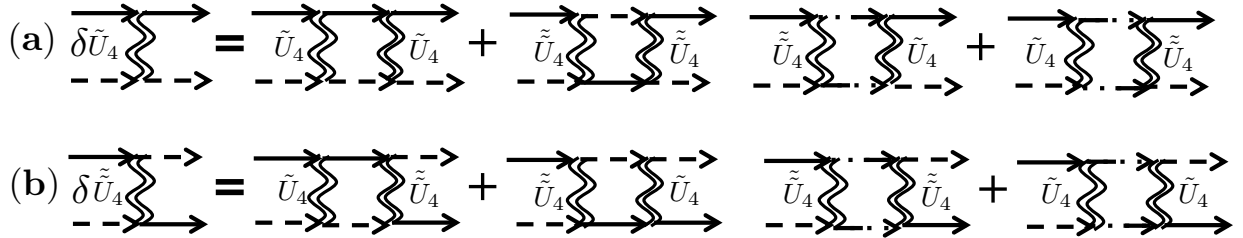


FIG. 8: Diagrammatic representation of the renormalizations of the interactions \tilde{U}_4 , (a) and $\tilde{\tilde{U}}_4$, (b), to second order in the interactions.

The energy and momentum integrations in (34) are performed using the expressions for the angular averages,

$$\langle \cos^4 \theta \rangle = \langle \sin^4 \theta \rangle = \frac{3}{8}, \quad \langle \cos^2 \theta \sin^2 \theta \rangle = \frac{1}{8}. \tag{37}$$

We further have

$$\begin{aligned} \int_{dk} \frac{d^2 \mathbf{k}}{4\pi^2} \int \frac{d\epsilon}{2\pi} G_{d(c)}(i\epsilon, \mathbf{k}) G_{d(c)}(-i\epsilon, -\mathbf{k}) &= \frac{dL}{4\pi} m_{c(d)}, \\ \int_{dk} \frac{d^2 \mathbf{k}}{4\pi^2} \int \frac{d\epsilon}{2\pi} G_{d(c)}(i\epsilon, \mathbf{k}) G_{c(d)}(-i\epsilon, -\mathbf{k}) &= \frac{dL}{4\pi} \frac{2m_c m_d}{m_c + m_d}. \end{aligned} \quad (38)$$

Substituting Eqs. (15), (35) and (36) into (34) and using (37) we obtain

$$\begin{aligned} 4\pi \frac{d\tilde{U}_4}{dL} &= -(\tilde{U}_4^2 + \tilde{\tilde{U}}_4^2) \left[\frac{1}{8}(m_c + m_d) + \frac{3}{8} \frac{4m_c m_d}{m_c + m_d} \right] - 2\tilde{U}_4 \tilde{\tilde{U}}_4 \frac{1}{8} \frac{(m_c - m_d)^2}{m_c + m_d}, \\ 4\pi \frac{d\tilde{\tilde{U}}_4}{dL} &= -2\tilde{U}_4 \tilde{\tilde{U}}_4 \left[\frac{1}{8}(m_c + m_d) + \frac{3}{8} \frac{4m_c m_d}{m_c + m_d} \right] - (\tilde{U}_4^2 + \tilde{\tilde{U}}_4^2) \frac{1}{8} \frac{(m_c - m_d)^2}{m_c + m_d}. \end{aligned} \quad (39)$$

It follows that

$$4\pi \frac{d(\tilde{U}_4 \pm \tilde{\tilde{U}}_4)}{dL} = -(\tilde{U}_4 \pm \tilde{\tilde{U}}_4)^2 \left[\frac{1}{8}(m_c + m_d) + \frac{3}{8} \frac{4m_c m_d}{m_c + m_d} \pm \frac{1}{8} \frac{(m_c - m_d)^2}{m_c + m_d} \right]. \quad (40)$$

Solving Eq. (40) we find that the interactions \tilde{U}_4 and $\tilde{\tilde{U}}_4$ flow to zero under pRG, provided at the bare level $\tilde{U}_4 > \tilde{\tilde{U}}_4$. Like before, this holds when $U' > J$. As this condition is supposed to be satisfied, we may safely set \tilde{U}_4 and $\tilde{\tilde{U}}_4$ to zero.

C. The third group of pRG equations

Finally we derive and solve the pRG equations obeyed by the third group of couplings shown in Fig. 6.

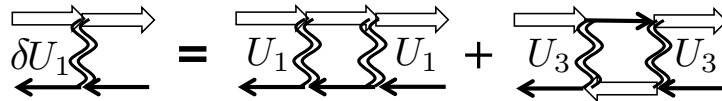


FIG. 9: Diagrammatic representation of the renormalizations of the interaction U_1 to second order in the interactions. The diagrams for \bar{U}_1 have the same form in terms of \bar{U}_1 and \bar{U}_3 .

The interaction U_1 flows due to renormalizations in the particle-hole channel. The corresponding diagrams are shown in Fig. 9. In analytical form we have

$$dU_1 = -(U_1^2 + U_3^2) \int_{dk} \frac{d^2 \mathbf{k}}{4\pi^2} \int \frac{d\epsilon}{2\pi} G_{d_1; d_1}(i\epsilon, \mathbf{k}) G_{f_1}(i\epsilon, \mathbf{k}). \quad (41)$$

Using Eq. (36) we re-express Green's functions in the orbital basis via the Green's functions in the band basis:

$$\int_{dk} \frac{d^2 \mathbf{k}}{4\pi^2} \int \frac{d\epsilon}{2\pi} G_{d_1; d_1}(i\epsilon, \mathbf{k}) G_{f_1}(i\epsilon, \mathbf{k}) = \int_{dk} \frac{d^2 \mathbf{k}}{4\pi^2} \int \frac{d\epsilon}{2\pi} [\cos^2 \theta_{\mathbf{k}} G_c(i\epsilon, \mathbf{k}) + \sin^2 \theta_{\mathbf{k}} G_d(i\epsilon, \mathbf{k})] G_{f_1}(i\epsilon, \mathbf{k}). \quad (42)$$

We further write,

$$\int_{dk} \frac{d^2 \mathbf{k}}{(2\pi)^2} \int \frac{d\epsilon}{2\pi} \cos^2 \theta G_c G_{f_1} = \int_{dk} \frac{k dk}{2\pi} \int \frac{d\theta}{2\pi} \cos^2 \theta \int \frac{d\epsilon}{2\pi} G_c(i\epsilon, \xi_c(k)) G_{f_1}(i\epsilon, \xi_{f_1}(k)) \quad (43)$$

As $\xi_c(k) < 0$ and $\xi_{f_1} > 0$ integration over the energy gives,

$$\int \frac{d\epsilon}{2\pi} \frac{1}{i\epsilon + |\xi_c(k)|} \frac{1}{i\epsilon - \xi_{f_1}(k)} = -\frac{1}{|\xi_c(k)| + \xi_{f_1}(k)}. \quad (44)$$

We then obtain using Eq. (15)

$$\int_{dk} \frac{d^2 \mathbf{k}}{(2\pi)^2} \int \frac{d\epsilon}{2\pi} \cos^2 \theta G_c G_{f_1} = -\frac{1}{4\pi} \frac{dk^2}{k^2} \int_0^{2\pi} \frac{d\theta}{\pi} \frac{\cos^2 \theta}{\frac{1}{m_c} + \frac{\cos^2 \theta}{m_x} + \frac{\sin^2 \theta}{m_y}} = -\frac{dL}{4\pi} A_1, \quad (45)$$

where we have defined

$$A_1 = \int_0^{2\pi} \frac{d\theta}{\pi} \frac{\cos^2 \theta}{\frac{1}{m_c} + \frac{\cos^2 \theta}{m_x} + \frac{\sin^2 \theta}{m_y}}. \quad (46)$$

Similarly

$$\int_{dk} \frac{d^2 \mathbf{k}}{(2\pi)^2} \int \frac{d\epsilon}{2\pi} \cos^2 \theta G_d G_{f_2} = -\frac{dL}{4\pi} A_2, \quad (47)$$

where we have introduced,

$$A_2 = \int_0^{2\pi} \frac{d\theta}{\pi} \frac{\sin^2 \theta}{\frac{1}{m_d} + \frac{\cos^2 \theta}{m_x} + \frac{\sin^2 \theta}{m_y}}. \quad (48)$$

We see that the momentum integral is still logarithmical $\int k d(k)/k^2$, this time because hole and electronic excitations have opposite signs of the dispersion. This does not require a true nesting, i.e. hole and electron masses do not have to be equal and electron dispersion does not have to be circular. Still, the logarithmical behavior in the particle-hole channel for momenta $k \ll \Lambda$ holds only if both pockets are tiny, i.e, both Fermi momenta are small. We also note that Eq. (44) contains an additional minus sign compared to the contribution from the particle-particle channel.

The pRG equation for U_1 is obtained by substituting Eqs. (45) and (47) into Eq. (41). This yields

$$4\pi \frac{dU_1}{dL} = (U_1^2 + U_3^2)A, \quad (49)$$

where

$$A = A_1 + A_2. \quad (50)$$

The pRG equation for the interaction \bar{U}_1 is obtained in a similar way and is

$$4\pi \frac{d\bar{U}_1}{dL} = (\bar{U}_1^2 + \bar{U}_3^2) \bar{A}, \quad (51)$$

where

$$\bar{A} = \bar{A}_1 + \bar{A}_2, \quad (52)$$

and

$$\bar{A}_1 = \int_0^{2\pi} \frac{d\theta}{\pi} \frac{\sin^2 \theta}{\frac{1}{m_c} + \frac{\cos^2 \theta}{m_x} + \frac{\sin^2 \theta}{m_y}}, \quad \bar{A}_2 = \int_0^{2\pi} \frac{d\theta}{\pi} \frac{\cos^2 \theta}{\frac{1}{m_d} + \frac{\cos^2 \theta}{m_x} + \frac{\sin^2 \theta}{m_y}}. \quad (53)$$

The interactions U_2 and \bar{U}_2 are also renormalized in the particle-hole channel. The corresponding diagrams are shown in Fig. 10.

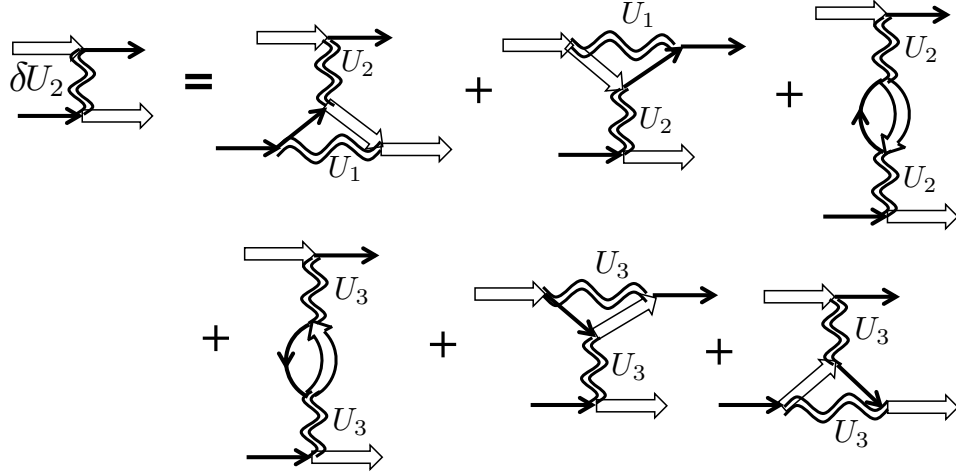


FIG. 10: Diagrammatic representation of the renormalizations of the interaction U_2 to second order in the interactions. The two contributions $\propto U_3^2$ in the second row cancel each other. The diagrams for \bar{U}_2 have the same form in terms of \bar{U}_1 and \bar{U}_2 .

The corresponding pRG equations are:

$$4\pi \frac{dU_2}{dL} = 2(U_1 U_2 - U_2^2) A, \quad (54)$$

and

$$4\pi \frac{d\bar{U}_2}{dL} = 2(\bar{U}_1 \bar{U}_2 - \bar{U}_2^2) A. \quad (55)$$

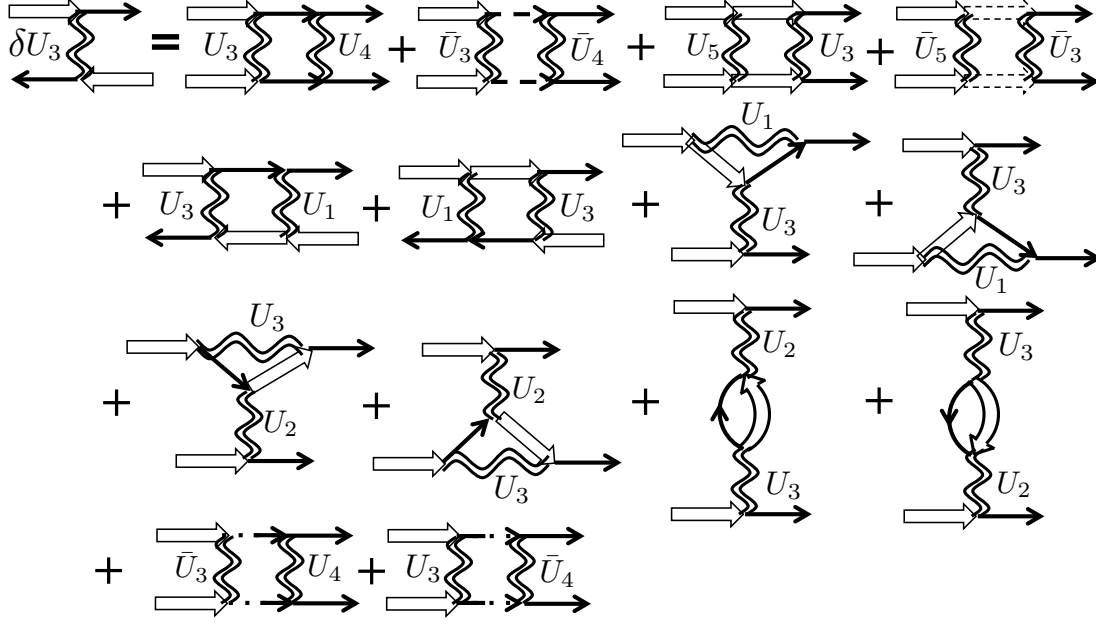


FIG. 11: Diagrammatic representation of the renormalizations of the interaction U_3 to second order in the interactions. The last two diagrams include the hole propagators, off-diagonal in the orbital index. There two diagrams vanish in the limit $m_c = m_d$. The diagrams for \bar{U}_3 are the same in terms of cross-products $\bar{U}_i U_j$.

The flow of U_3 is due to renormalizations in both particle-hole and particle-particle channels. The corresponding diagrams are shown in Fig. 11. As is clear from the Fig. 11, there are three contributions to the renormalization of U_3 :

$$dU_3 = d_h U_3 + d_e U_3 + d_{eh} U_3. \quad (56)$$

Here $d_h U_3$ is the contribution to dU_3 from integration over the hole momenta in the particle-particle channel, $d_e U_3$ is the contribution to dU_3 from integration over the electron momenta in particle-particle channel, and $d_{h,e} U_3$ is the contribution originating from the integration over both electron and hole momenta in the particle-hole channel. We start with the electronic contribution:

$$d_e U_3 = -(U_5 U_3 + \bar{U}_5 \bar{U}_3) \int_{dk} \frac{d^2 \mathbf{k}}{(2\pi)^2} \int \frac{d\epsilon}{2\pi} G_{f1,2}(\mathbf{k}, \epsilon) G_{f1,2}(-\mathbf{k}, -\epsilon). \quad (57)$$

We have

$$\begin{aligned} \int_{dL} \frac{d^2 k}{4\pi^2} \int \frac{d\epsilon}{2\pi} G_{f_1}(i\epsilon, \epsilon_{f_1}(k)) G_{f_1}(-i\epsilon, \epsilon_{f_1}(-k)) &= \int_{k-dk}^k \frac{k dk}{2\pi} \int \frac{d\phi}{2\pi} \frac{1}{2\xi_{f_1}} \\ &= \int_{k-dk}^k \frac{k dk}{2\pi} \int \frac{d\phi}{2\pi} \frac{1}{k^2 [\cos^2 \theta / m_x + \sin^2 \theta / m_y]} = \frac{dL}{4\pi} \sqrt{m_x m_y}. \end{aligned} \quad (58)$$

As a result, Eq. (57) takes the form,

$$4\pi \frac{d_e U_3}{dL} = -(U_5 U_3 + \bar{U}_5 \bar{U}_3) A_e, \quad (59)$$

where

$$A_e = \sqrt{m_x m_y}. \quad (60)$$

The contribution from integrating over momenta of hole excitations in the particle-particle channel is

$$\begin{aligned} d_h U_3 &= -U_3 U_4 \int_{dk} \frac{d^2 \mathbf{k}}{4\pi^2} \int \frac{d\epsilon}{2\pi} G_{d_1; d_1}(i\epsilon, \mathbf{k}) G_{d_1; d_1}(-i\epsilon, -\mathbf{k}) \\ &\quad - \bar{U}_3 \bar{U}_4 \int_{dk} \frac{d^2 \mathbf{k}}{4\pi^2} \int \frac{d\epsilon}{2\pi} G_{d_2; d_2}(i\epsilon, \mathbf{k}) G_{d_2; d_2}(-i\epsilon, -\mathbf{k}) \\ &\quad - U_3 \bar{U}_4 \int_{dk} \frac{d^2 \mathbf{k}}{4\pi^2} \int \frac{d\epsilon}{2\pi} G_{d_1; d_2}(i\epsilon, \mathbf{k}) G_{d_1; d_2}(-i\epsilon, -\mathbf{k}) \\ &\quad - \bar{U}_3 U_4 \int_{dk} \frac{d^2 \mathbf{k}}{4\pi^2} \int \frac{d\epsilon}{2\pi} G_{d_2; d_1}(i\epsilon, \mathbf{k}) G_{d_2; d_1}(-i\epsilon, -\mathbf{k}). \end{aligned} \quad (61)$$

Here the last two terms are graphically presented by the last two diagrams in the Fig. 11. The integrations in the first two terms are entirely analogous to those in Eq. (34) and we just quote the result,

$$\int_{dk} \frac{d^2 \mathbf{k}}{4\pi^2} \int \frac{d\epsilon}{2\pi} G_{d_1, 2; d_1, 2}(i\epsilon, \mathbf{k}) G_{d_1, 2; d_1, 2}(-i\epsilon, -\mathbf{k}) = \frac{dL}{4\pi} A_h, \quad (62)$$

where

$$A_h = \frac{3}{8}(m_c + m_d) + \frac{1}{8} \frac{4m_c m_d}{m_c + m_d}. \quad (63)$$

The two remaining integrals yield

$$\int_{dk} \frac{d^2 \mathbf{k}}{4\pi^2} \int \frac{d\epsilon}{2\pi} G_{d_1, 2; d_2, 1}(i\epsilon, \mathbf{k}) G_{d_1, 2; d_2, 1}(-i\epsilon, -\mathbf{k}) = \frac{dL}{4\pi} A_h^-, \quad (64)$$

where

$$A_h^- = \frac{1}{8} \frac{(m_c - m_d)^2}{m_c + m_d}. \quad (65)$$

We have therefore

$$4\pi \frac{d_h U_3}{dL} = -(U_3 U_4 + \bar{U}_3 \bar{U}_4) A_h - (U_3 \bar{U}_4 + \bar{U}_3 U_4) A_h^- . \quad (66)$$

Finally, $d_{eh} U_3$ contains the same integrals as dU_2 . Borrowing the results we obtain

$$4\pi \frac{d_{eh} U_3}{dL} = (4U_3 U_1 - 2U_2 U_3) A . \quad (67)$$

Adding the contributions (59), (67) and (66) we obtain

$$4\pi \frac{dU_3}{dL} = -(U_5 U_3 + \bar{U}_5 \bar{U}_3) A_e - (U_3 U_4 + \bar{U}_3 \bar{U}_4) A_h - (U_3 \bar{U}_4 + \bar{U}_3 U_4) A_h^- + (4U_3 U_1 - 2U_2 U_3) A . \quad (68)$$

The equations for the remaining five amplitudes are obtained in a similar fashion. We list these five equations below together with the equations that we already obtained:

$$\begin{aligned} 4\pi \dot{U}_1 &= AU_1^2 + AU_3^2 \\ 4\pi \dot{\bar{U}}_1 &= \bar{A}\bar{U}_1^2 + \bar{A}\bar{U}_3^2 \\ 4\pi \dot{U}_2 &= 2AU_1 U_2 - 2AU_2^2 \\ 4\pi \dot{\bar{U}}_2 &= 2\bar{A}\bar{U}_1 \bar{U}_2 - 2\bar{A}\bar{U}_2^2 \\ 4\pi \dot{U}_3 &= -A_h U_3 U_4 - A_h \bar{U}_3 \bar{U}_4 - A_h^- U_3 \bar{U}_4 - A_h^- \bar{U}_3 U_4 + 4AU_3 U_1 - 2AU_2 U_3 - A_e U_5 U_3 - A_e \bar{U}_5 \bar{U}_3 \\ 4\pi \dot{\bar{U}}_3 &= -A_h \bar{U}_3 U_4 - A_h U_3 \bar{U}_4 - A_h^- U_3 U_4 - A_h^- \bar{U}_3 \bar{U}_4 + 4\bar{A}\bar{U}_3 \bar{U}_1 - 2\bar{A}\bar{U}_2 \bar{U}_3 - A_e U_5 \bar{U}_3 - A_e \bar{U}_5 U_3 \\ 4\pi \dot{U}_4 &= -A_h U_4^2 - A_h \bar{U}_4^2 - 2A_h^- U_4 \bar{U}_4 - A_e U_3^2 - A_e \bar{U}_3^2 \\ 4\pi \dot{\bar{U}}_4 &= -2A_h U_4 \bar{U}_4 - A_h^- U_4^2 - A_h^- \bar{U}_4^2 - 2A_e U_3 \bar{U}_3 \\ 4\pi \dot{U}_5 &= -A_e U_5^2 - A_e \bar{U}_5^2 - A_h U_3^2 - A_h \bar{U}_3^2 - 2A_h^- U_3 \bar{U}_3 \\ 4\pi \dot{\bar{U}}_5 &= -2A_e U_5 \bar{U}_5 - 2A_h U_3 \bar{U}_3 - A_h^- U_3^2 - A_h^- \bar{U}_3^2 . \end{aligned} \quad (69)$$

We now introduce the dimensionless couplings

$$\begin{aligned} u_{1,2} &= \frac{A}{4\pi} U_{1,2} , & u_3 &= \frac{A}{4\pi} C U_3 , & \bar{u}_{1,2} &= \frac{\bar{A}}{4\pi} \bar{U}_{1,2} , & \bar{u}_3 &= \frac{\bar{A}}{4\pi} \bar{C} \bar{U}_3 , \\ u_4 &= \frac{A_h}{4\pi} U_4 , & \bar{u}_4 &= \frac{A_h}{4\pi} \bar{U}_4 , & u_5 &= \frac{A_e}{4\pi} U_5 , & \bar{u}_5 &= \frac{A_e}{4\pi} \bar{U}_5 , \end{aligned} \quad (70)$$

and the parameters

$$C = \frac{\sqrt{A_h A_e}}{A} , \quad \bar{C} = \frac{\sqrt{A_h A_e}}{\bar{A}} . \quad (71)$$

Re-expressing (69) in terms of dimensionless couplings from Eq. (70) and the parameters C and \bar{C} , we obtain

$$\begin{aligned}
\dot{u}_1 &= u_1^2 + u_3^2/C^2 \\
\dot{\bar{u}}_1 &= \bar{u}_1^2 + \bar{u}_3^2/\bar{C}^2 \\
\dot{u}_2 &= 2u_1u_2 - 2u_2^2 \\
\dot{\bar{u}}_2 &= 2\bar{u}_1\bar{u}_2 - 2\bar{u}_2^2 \\
\dot{u}_3 &= -u_3u_4 - (C/\bar{C})\bar{u}_3\bar{u}_4 - (A_h^-/A_h)u_3\bar{u}_4 - (A_h^-/A_h)(C/\bar{C})\bar{u}_3u_4 \\
&\quad + 4u_3u_1 - 2u_2u_3 - u_5u_3 - (C/\bar{C})\bar{u}_5\bar{u}_3 \\
\dot{\bar{u}}_3 &= -\bar{u}_3u_4 - (\bar{C}/C)u_3\bar{u}_4 - (A_h^-/A_h)(\bar{C}/C)u_3u_4 - (A_h^-/A_h)\bar{u}_3\bar{u}_4 \\
&\quad + 4\bar{u}_3\bar{u}_1 - 2\bar{u}_2\bar{u}_3 - u_5\bar{u}_3 - (\bar{C}/C)\bar{u}_5u_3 \\
\dot{u}_4 &= -u_4^2 - \bar{u}_4^2 - 2(A_h^-/A_h)u_4\bar{u}_4 - u_3^2 - \bar{u}_3^2 \\
\dot{\bar{u}}_4 &= -2u_4\bar{u}_4 - (A_h^-/A_h)u_4^2 - (A_h^-/A_h)\bar{u}_4^2 - 2u_3\bar{u}_3 \\
\dot{u}_5 &= -u_5^2 - \bar{u}_5^2 - u_3^2 - \bar{u}_3^2 - 2(A_h^-/A_h)u_3\bar{u}_3 \\
\dot{\bar{u}}_5 &= -2u_5\bar{u}_5 - 2u_3\bar{u}_3 - (A_h^-/A_h)u_3^2 - (A_h^-/A_h)\bar{u}_3^2.
\end{aligned} \tag{72}$$

We further notice that in 122 systems, the masses m_x and m_y get interchanged once k_z changes to $\rightarrow k_z + \pi$. Averaging over k_z then makes the parameters A_1 and \bar{A}_1 equal. The pRG equations can be further simplified by setting $m_c = m_d = m_h$. Then

$$A = \bar{A} = \frac{2m_em_h}{m_e + m_h}, \quad A_e = m_e, \quad A_h = m_h, \quad A_h^- = 0, \quad C = \bar{C} = \frac{m_e + m_h}{2\sqrt{m_em_h}}. \tag{73}$$

Under this approximation, the set of pRG Eqs. (72) simplifies to

$$\begin{aligned}
\dot{u}_1 &= u_1^2 + u_3^2/C^2 \\
\dot{\bar{u}}_1 &= \bar{u}_1^2 + \bar{u}_3^2/C^2 \\
\dot{u}_2 &= 2u_1u_2 - 2u_2^2 \\
\dot{\bar{u}}_2 &= 2\bar{u}_1\bar{u}_2 - 2\bar{u}_2^2 \\
\dot{u}_3 &= -u_3u_4 - \bar{u}_3\bar{u}_4 + 4u_3u_1 - 2u_2u_3 - u_5u_3 - \bar{u}_5\bar{u}_3 \\
\dot{\bar{u}}_3 &= -\bar{u}_3u_4 - u_3\bar{u}_4 + 4\bar{u}_3\bar{u}_1 - 2\bar{u}_2\bar{u}_3 - u_5\bar{u}_3 - \bar{u}_5u_3 \\
\dot{u}_4 &= -u_4^2 - \bar{u}_4^2 - u_3^2 - \bar{u}_3^2 \\
\dot{\bar{u}}_4 &= -2u_4\bar{u}_4 - 2u_3\bar{u}_3 \\
\dot{u}_5 &= -u_5^2 - \bar{u}_5^2 - u_3^2 - \bar{u}_3^2 \\
\dot{\bar{u}}_5 &= -2u_5\bar{u}_5 - 2u_3\bar{u}_3.
\end{aligned} \tag{74}$$

These are the equations which we presented in the main text. They are more general than the ones obtained earlier (Refs. [5, 32, 33]), which neglected orbital content of low-energy excitations. The earlier pRG equations are reproduced if we set $\bar{u}_i = 0$ from the beginning and also set $C = 1$, i.e., assume that excitations near hole and electron pockets have equal masses.

III. SOLUTION OF RG EQUATIONS

In this section we analyse the pRG Eq. (74). For completeness and for comparison with earlier works we first set bare values of all $\bar{u}_i = 0$. Eqs. (74) then show that all \bar{u}_i remain zero in the pRG flow. We consider the fixed trajectory for arbitrary $C \geq 1$ and show the earlier results are recovered in the limit $C = 1$.

Next, we show that the trajectories with $\bar{u}_i = 0$, $i = 1 - 5$ are unstable already for arbitrary small non-zero bare values of \bar{u}_i and find the fixed trajectory for the full model. We show that the only stable fixed trajectory is the one with $u_i = \bar{u}_i$, $i = 1 - 5$.

A. The fixed trajectories with $\bar{u}_i = 0$, $i = 1 - 5$.

these amplitudes remain zero under the pRG flow, as follows from Eq. (74). The remaining pRG equations are

$$\begin{aligned} \dot{u}_1 &= u_1^2 + u_3^2/C^2 \\ \dot{u}_2 &= -2u_2^2 + 2u_1u_2 \\ \dot{u}_3 &= [4u_1 - 2u_2 - (u_4 + u_5)]u_3 \\ \dot{u}_4 &= -u_4^2 - u_3^2 \\ \dot{u}_5 &= -u_5^2 - u_3^2 \end{aligned} \tag{75}$$

For $C = 1$, the equations are the same as in Refs. [5, 33]. Notice that, if $u_4 = u_5$ at the bare level, they remain equal under pRG. For simplicity we set $u_4 = u_5$.

The fixed trajectories are the solutions of (75) to which the system flows at large L . One can easily verified that such solutions satisfy

$$u_2 = \gamma_2 u_1, u_3 = \gamma_3 u_1, u_4 = \gamma_4 u_1 \tag{76}$$

with constant γ_i , i.e., the ratios of the couplings tend to finite values under pRG. To obtain γ_i we substitute (76) into (75). This gives

$$\dot{u}_1 = u_1^2 (1 + \gamma_3^2/C^2) \tag{77}$$

and

$$\begin{aligned} \gamma_2 (1 + \gamma_3^2/C^2) &= \gamma_2 [2 - 2\gamma_2] \\ \gamma_3 (1 + \gamma_3^2/C^2) &= \gamma_3 [4 - 2\gamma_2 - 2\gamma_4] \\ \gamma_4 (1 + \gamma_3^2/C^2) &= -(\gamma_4^2 + \gamma_3^2). \end{aligned} \tag{78}$$

The last equation implies that $\gamma_4 < 0$, and we write $\gamma_4 = -|\gamma_4|$. The solution with all $\gamma_i \neq 0$ does not exist, as one can easily verify. However, the solutions with either $\gamma_2 = 0$ and/or $\gamma_3 = 0$ do exist.

Consider first the case $\gamma_3 = 0$, $\gamma_2 \neq 0$. In this case the second equation (78) should be disregarded. The other two equations give $\gamma_2 = 1/2$ and $\gamma_4 = -1$. Hence, along the fixed trajectory

$$u_1(L) = \frac{1}{L_0 - L}, \quad \gamma_2 = 1/2, \gamma_3 = 0, \gamma_4 = -1. \tag{79}$$

This fixed trajectory describes the $u_3 = 0$ separatrix. The solution exists per se, but the fixed trajectory is unstable in the sense that once bare u_3 is arbitrary small but finite, the pRG trajectory runs out of Eq. (79). Indeed, the pRG equation for u_3 in (75), linearized in the proximity of the solution (79), gives $\dot{u}_3 = [4u_1 - 2u_2 - (u_4 + u_5)]u_3 \approx 5u_1u_3$. Because u_1 is positive, u_3 increases by magnitude, no matter whether its bare value is positive or negative. The fixed trajectory with $\gamma_2 = 0, \gamma_3 = 0, \gamma_4 = -1$ is equally unstable.

Consider next the case $\gamma_3 \neq 0$, and $\gamma_2 = 0$. In this case the first equation in (78) should be disregarded. The remaining three equations give

$$\begin{aligned} 4 + 2|\gamma_4| &= 1 + \gamma_3^2/C^2 \\ 1 + \gamma_3^2/C^2 &= |\gamma_4| + \gamma_3^2/|\gamma_4|. \end{aligned} \quad (80)$$

Solving this set we obtain

$$\gamma_2 = 0, \quad \gamma_3 = \pm C \left[-1 + 2C^2 + 2\sqrt{(2 - C^2)^2 + 3C^2} \right]^{1/2}, \quad \gamma_4 = (2 - C^2) - \sqrt{(2 - C^2)^2 + 3C^2}. \quad (81)$$

For $C = 1$ we recover the earlier results, $\gamma_2 = 0, \gamma_3 = \sqrt{5}, \gamma_4 = -1$ [5]. The initial conditions in our model are such that bare $u_3 > 0$, hence we choose the plus sign in the second equation in (81). Along the fixed trajectory (81),

$$\dot{u}_1(L) = (u_1(L))^2 \left(1 + \left(\frac{\gamma_3}{C} \right)^2 \right). \quad (82)$$

Solving this equation, we obtain

$$u_1(L) = \frac{1}{1 + \gamma_3^2/C^2} \frac{1}{L_0 - L}, \quad (83)$$

The scale L_0 cannot be explicitly obtained by solving pRG equations only along the fixed trajectory. Roughly,

$$L_0 = 1/[u_1(0)(1 + \gamma_3^2/C^2)]. \quad (84)$$

We remark that the condition $\gamma_2 = 0$ implies that u_2/u_1 tends to zero under pRG, but does not necessarily imply that u_2 itself tends to zero under pRG. In fact, by going beyond the leading approximation, one finds that u_2 also increases as L approaches L_0 , but scales as

B. The fixed trajectory in the full model with non-zero bare values of u_i and \bar{u}_i

We first show the trajectory with $\bar{u}_i = 0$, $i = 1 - 5$, found in Sec. III A, is unstable. To see this we perform a linear stability analysis around the fixed trajectory with $\bar{u}_i = 0$, Eq. (76), (81), assuming that the bare values of \bar{u}_i are small but finite. From the second and fourth equations in the set (74) we see that, to the linear order, we still have $\dot{\bar{u}}_1 = \dot{\bar{u}}_2 = 0$. For simplicity we also set have $\bar{u}_4 = \bar{u}_5$. The remaining two equations on \bar{u}_3 and \bar{u}_4 are

$$\begin{aligned}\dot{\bar{u}}_3 &\approx -2u_4\bar{u}_3 - 2u_3\bar{u}_4 \\ \dot{\bar{u}}_4 &\approx -2u_3\bar{u}_3 - 2u_4\bar{u}_4.\end{aligned}\tag{85}$$

Along the fixed trajectory, Eq. (85) can be written in the matrix form as

$$\begin{bmatrix} \dot{\bar{u}}_3 \\ \dot{\bar{u}}_4 \end{bmatrix} = 2u_1 \hat{M} \begin{bmatrix} \bar{u}_3 \\ \bar{u}_4 \end{bmatrix},\tag{86}$$

where

$$\hat{M} = \begin{bmatrix} -\gamma_4 & -\gamma_3 \\ -\gamma_3 & -\gamma_4 \end{bmatrix}.\tag{87}$$

This matrix is guaranteed to have at least one positive eigenvalue because $\gamma_4 < 0$. Because u_1 is positive, this means that the trajectory with \bar{u}_i , $i = 1 - 5$ is unstable.

We next conjecture that the only stable fixed trajectory of the full set of pRG equations is the one with

$$u_i = \bar{u}_i, i = 1 - 5, \quad u_4 = u_5.\tag{88}$$

Note that if Eq. (88) is satisfied at the bare level, it holds under pRG. Along the phase trajectory of Eq. (88) the couplings u_i , $i = 1 - 4$ satisfy

$$\begin{aligned}\dot{u}_1 &= u_1^2 + u_3^2/C^2 \\ \dot{u}_2 &= 2u_1u_2 - 2u_2^2 \\ \dot{u}_3 &= 4u_3u_1 - 2u_2u_3 - 4u_3u_4 \\ \dot{u}_4 &= -2u_4^2 - 2u_3^2\end{aligned}\tag{89}$$

We again assume that the ratios of the couplings tend to finite values as the system approaches the fixed trajectory and write

$$u_2 = \gamma_2 u_1, u_3 = \gamma_3 u_1, u_4 = \gamma_4 u_1.\tag{90}$$

Substituting this into (89) we obtain

$$\dot{u}_1 = u_1^2 \left(1 + \gamma_3^2/C^2\right) \quad (91)$$

and

$$\begin{aligned} \gamma_2 \left(1 + \gamma_3^2/C^2\right) &= \gamma_2(2 - 2\gamma_2) \\ \gamma_3 \left(1 + \gamma_3^2/C^2\right) &= \gamma_3[4(1 - \gamma_4 - 2\gamma_2)] \\ \gamma_4 \left(1 + \gamma_3^2/C^2\right) &= -2 \left(\gamma_4^2 + \gamma_3^2\right). \end{aligned} \quad (92)$$

We again see that (i) γ_4 must be negative, i.e. $\gamma_4 = -|\gamma_4|$, and (ii) that the solution with both $\gamma_2 \neq 0$ and $\gamma_3 \neq 0$ does not exist. as in this case the first and the second equations in (92) give $\gamma_4 = 1/2$, inconsistent with the third equation. Hence either γ_2 or γ_3 , or both, must vanish.

For $\gamma_2 = 0$ and $\gamma_3 \neq 0$ we obtain from (92)

$$\gamma_3 = \pm C \sqrt{8C^2 - 1 + 4\sqrt{1 - C^2 + 4C^4}}, \gamma_4 = 1 - 2C^2 - \sqrt{1 - C^2 + 4C^4}. \quad (93)$$

For $C = 1$ this gives $\gamma_2 = 0$, $\gamma_3 = \sqrt{15}$, $\gamma_4 = -3$. We verified, both numerically and analytically that this fixed trajectory is stable. the condition $\gamma_2 = 0$ actually means that u_2 and \bar{u}_2 scale as $u_2 = u_{20}/(L_0 - L)^p$, $\bar{u}_2 = \bar{u}_{20}/(L_0 - L)^p$, with $p = 2/(1 + (\gamma_3/C)^2) < 1$, such that u_2/u_1 and \bar{u}_2/\bar{u}_1 both tend to zero. At the same time, the prefactors u_{20} and \bar{u}_{20} depend on initial conditions and in general are not equal, i.e., the ratio u_2/\bar{u}_2 does not become equal to one along the fixed trajectory.

For $\gamma_2 \neq 0$ and $\gamma_3 = 0$ we obtain from (92)

$$\gamma_2 = 1/2, \gamma_3 = 0, \gamma_4 = -1/2. \quad (94)$$

This fixed trajectory exists pr se but is unstable because at small deviations from $\gamma_3 = 0$ (and hence $u_3 = 0$) we have $\dot{u}_3 \approx u_1 u_3$, hence if u_3 is initially non-zero, it grows, i.e., the system moves away from the trajectory specified by (94).

Finally, if we set $\gamma_2 = \gamma_3 = 0$, we obtain fixed trajectory with

$$\gamma_2 = 0, \gamma_3 = 0, \gamma_4 = -1/2. \quad (95)$$

This trajectory is also unstable because once we make γ_2 (and, hence, u_2) small but non-zero, u_2 will flow according to $\dot{u}_2 \approx 2u_2 u_1$ and keep increasing.

We see therefore that the only stable fixed trajectory is the one specified by Eq. (93). The running coupling u_1 satisfies the same equation $\dot{u}_1 = u_1^2(1 + (\gamma_3/C)^2)$ as for the case when $\bar{u}_i = 0$, and its flow is given by Eq. (83).

IV. SDW, SC, AND ORBITAL CHANNELS: VERTICES AND RELEVANT INTERACTIONS

A. Interaction channels

The tetragonal symmetry further allows us to decompose the running interactions in Eq. (20) into different channels. To achieve this goal we construct bilinear fermion operators that transform irreducibly under the symmetry group of the lattice. We consider separately the bilinear combinations in the particle-hole channel at zero momentum and at momenta $\mathbf{Q}_{1,2}$, and the bilinear combinations in the particle-particle channel at zero total momentum.

1. Bilinear fermion combinations in the charge and spin particle-hole channels at large momentum transfer

The two possible order parameters which describe charge-density-wave (CDW) order with momenta $(\pi, 0)$ and $(0, \pi)$ are

$$\delta_{1,2}^r = f_{1,2}^\dagger d_{1,2} + d_{1,2}^\dagger f_{1,2}, \quad \delta_{1,2}^i = i(f_{1,2}^\dagger d_{1,2} - d_{1,2}^\dagger f_{1,2}). \quad (96)$$

Another two possible charge order with large momentum transfer describe anti-ferro-orbital order. The corresponding order parameters are

$$\bar{\delta}_{1,2}^r = f_{1,2}^\dagger d_{2,1} + d_{2,1}^\dagger f_{1,2}, \quad \bar{\delta}_{1,2}^i = i(f_{1,2}^\dagger d_{2,1} - d_{2,1}^\dagger f_{1,2}). \quad (97)$$

These order parameters differ from the ones in Eqs. (96) because they are off-diagonal in the orbital index.

The four possible SDW order parameters with the same momenta are

$$\mathbf{s}_{1,2}^r = f_{1,2}^\dagger \boldsymbol{\sigma} d_{1,2} + d_{1,2}^\dagger \boldsymbol{\sigma} f_{1,2}, \quad \mathbf{s}_{1,2}^i = i(f_{1,2}^\dagger \boldsymbol{\sigma} d_{1,2} - d_{1,2}^\dagger \boldsymbol{\sigma} f_{1,2}), \quad (98)$$

$$\bar{\mathbf{s}}_{1,2}^r = f_{1,2}^\dagger \boldsymbol{\sigma} d_{2,1} + d_{1,2}^\dagger \boldsymbol{\sigma} f_{2,1}, \quad \bar{\mathbf{s}}_{1,2}^i = i(f_{1,2}^\dagger \boldsymbol{\sigma} d_{2,1} - d_{1,2}^\dagger \boldsymbol{\sigma} f_{2,1}). \quad (99)$$

The components of Eq. (20) which describe the interactions in CDW and SDW channels are

$$\begin{aligned} H_{\delta,\pi} = & \frac{1}{8}(-U_1 + 2U_2 + U_3) [\delta_1^r \delta_1^r + \delta_2^r \delta_2^r] + \frac{1}{8}(-U_1 + 2U_2 - U_3) [\delta_1^i \delta_1^i + \delta_2^i \delta_2^i] \\ & + \frac{1}{8}(-\bar{U}_1 + 2\bar{U}_2 + \bar{U}_3) [\bar{\delta}_1^r \bar{\delta}_1^r + \bar{\delta}_2^r \bar{\delta}_2^r] + \frac{1}{8}(-\bar{U}_1 + 2\bar{U}_2 - \bar{U}_3) [\bar{\delta}_1^i \bar{\delta}_1^i + \bar{\delta}_2^i \bar{\delta}_2^i] \end{aligned} \quad (100)$$

and

$$\begin{aligned} H_{s,\pi} = & \frac{1}{8}(-U_1 - U_3) [\mathbf{s}_1^r \mathbf{s}_1^r + \mathbf{s}_2^r \mathbf{s}_2^r] + \frac{1}{8}(-U_1 + U_3) [\mathbf{s}_1^i \mathbf{s}_1^i + \mathbf{s}_2^i \mathbf{s}_2^i] \\ & + \frac{1}{8}(-\bar{U}_1 - \bar{U}_3) [\bar{\mathbf{s}}_1^r \bar{\mathbf{s}}_1^r + \bar{\mathbf{s}}_2^r \bar{\mathbf{s}}_2^r] + \frac{1}{8}(-\bar{U}_1 + \bar{U}_3) [\bar{\mathbf{s}}_1^i \bar{\mathbf{s}}_1^i + \bar{\mathbf{s}}_2^i \bar{\mathbf{s}}_2^i]. \end{aligned} \quad (101)$$

2. Bilinear fermion combinations in the particle-particle channel

We focus on the singlet pairing with zero total momentum. We introduce the notations

$$\kappa_{\mu\mu'}^f = f_{\mu\uparrow} f_{\mu'\downarrow}, \quad \kappa_{\mu\mu'}^d = d_{\mu\uparrow} d_{\mu'\downarrow}. \quad (102)$$

The fermion bilinear combinations are classified as follows,

$$\begin{aligned} \kappa_{A_1}^{f(d)} &= \kappa_{11}^{f(d)} + \kappa_{22}^{f(d)} \\ \kappa_{B_1}^{f(d)} &= \kappa_{11}^{f(d)} - \kappa_{22}^{f(d)} \\ \kappa_{B_2}^{f(d)} &= \kappa_{12}^{f(d)} + \kappa_{21}^{f(d)}. \end{aligned} \quad (103)$$

Note that the A_{2g} combination, $\kappa_{A_2}^{f(d)} = \kappa_{12}^{f(d)} - \kappa_{21}^{f(d)}$ vanishes as it is odd in the orbital index. The interaction component in the Cooper channel is obtained by setting $\mathbf{k}_1 = -\mathbf{k}_2$ in Eq. (20). Expressing Eq. (20) in terms of the combinations (103) we obtain

$$H_\kappa = H_{\kappa_{A_1}} + H_{\kappa_{B_1}} + H_{\kappa_{B_2}}, \quad (104)$$

$$H_{\kappa_{A_1}} = \frac{1}{2}(U_5 + \bar{U}_5) [\kappa_{A_1}^f]^\dagger \kappa_{A_1}^f + \frac{1}{2}(U_4 + \bar{U}_4) [\kappa_{A_1}^d]^\dagger \kappa_{A_1}^d + \frac{1}{2}(U_3 + \bar{U}_3) ([\kappa_{A_1}^f]^\dagger \kappa_{A_1}^d + h.c.) \quad (105)$$

$$H_{\kappa_{B_1}} = \frac{1}{2}(U_5 - \bar{U}_5) [\kappa_{B_1}^f]^\dagger \kappa_{B_1}^f + \frac{1}{2}(U_4 - \bar{U}_4) [\kappa_{B_1}^d]^\dagger \kappa_{B_1}^d + \frac{1}{2}(U_3 - \bar{U}_3) ([\kappa_{B_1}^f]^\dagger \kappa_{B_1}^d + h.c.) \quad (106)$$

$$H_{\kappa_{B_2}} = \frac{1}{2}(\tilde{U}_5 + \tilde{\bar{U}}_5) [\kappa_{B_2}^f]^\dagger \kappa_{B_2}^f + \frac{1}{2}(\tilde{U}_4 + \tilde{\bar{U}}_4) [\kappa_{B_2}^f]^\dagger \kappa_{B_2}^f \quad (107)$$

3. Bilinear fermion combinations in particle-hole charge channel with zero momentum transfer

The bilinear combinations of fermions with zero momentum transfer in the particle-hole charge channel are

$$\rho_{\mu\mu'}^f = \sum_{\sigma} f_{\mu\sigma}^{\dagger} f_{\mu'\sigma}, \quad \rho_{\mu\mu'}^d = \sum_{\sigma} d_{\mu\sigma}^{\dagger} d_{\mu'\sigma} \quad (108)$$

These combinations form reducible representations of the D_{4h} group, separately for electrons, f and holes, d (Ref. [41]). All bilinear combinations are even under inversion, hence we only consider one-dimensional (even) irreducible presentations of the D_{4h} group: A_{1g} , A_{2g} , B_{1g} and B_{2g} .

The combinations

$$\begin{aligned} \rho_{A_1}^{f(d)} &= \rho_{11}^{f(d)} + \rho_{22}^{f(d)} \\ \rho_{B_1}^{f(d)} &= \rho_{11}^{f(d)} - \rho_{22}^{f(d)} \\ \rho_{A_2}^{f(d)} &= \rho_{12}^{f(d)} - \rho_{21}^{f(d)} \\ \rho_{B_2}^{f(d)} &= \rho_{12}^{f(d)} + \rho_{21}^{f(d)} \end{aligned} \quad (109)$$

transform as A_{1g} , B_{1g} , A_{2g} , B_{2g} respectively.

To obtain the interactions in the particle-hole charge channel at zero momentum transfer (the ones which renormalize bilinear combinations in (109) we set $\mathbf{k}_1 = \mathbf{k}_2$ or $\mathbf{k}_1 = \mathbf{k}_4$ in Eq. (20). Expressing Eq. (20) in terms of the combinations (109) we obtain

$$H_{\rho} = H_{\rho_{A_1}} + H_{\rho_{A_2}} + H_{\rho_{B_1}} + H_{\rho_{B_2}}, \quad (110)$$

where

$$H_{\rho_{A_1}} = \frac{1}{8}(U_5 + 2\tilde{U}_5 - \tilde{\tilde{U}}_5)[\rho_{A_1}^f]^2 + \frac{1}{8}(U_4 + 2\tilde{U}_4 - \tilde{\tilde{U}}_4)[\rho_{A_1}^d]^2 + \frac{1}{4}\rho_{A_1}^f \rho_{A_1}^d (2U_1 - U_2 + 2\bar{U}_1 - \bar{U}_2) \quad (111)$$

$$H_{\rho_{B_1}} = \frac{1}{8}(U_5 - 2\tilde{U}_5 + \tilde{\tilde{U}}_5)[\rho_{B_1}^f]^2 + \frac{1}{8}(U_4 - 2\tilde{U}_4 + \tilde{\tilde{U}}_4)[\rho_{B_1}^d]^2 + \frac{1}{4}\rho_{B_1}^f \rho_{B_1}^d (2U_1 - U_2 - 2\bar{U}_1 + \bar{U}_2) \quad (112)$$

$$H_{\rho_{A_2}} = \frac{1}{8}(\bar{U}_5 - 2\tilde{\tilde{U}}_5 + \tilde{U}_5)[\rho_{A_2}^f]^2 + \frac{1}{8}(\bar{U}_4 - 2\tilde{\tilde{U}}_4 + \tilde{U}_4)[\rho_{A_2}^d]^2 \quad (113)$$

$$H_{\rho_{B_2}} = \frac{1}{8}(\bar{U}_5 + 2\tilde{\tilde{U}}_5 - \tilde{U}_5)[\rho_{B_2}^f]^2 + \frac{1}{8}(\bar{U}_4 + 2\tilde{\tilde{U}}_4 - \tilde{U}_4)[\rho_{B_2}^d]^2 \quad (114)$$

B. pRG equations for the flow of vertex functions in different channels

We now use the solutions of pRG equations for the running couplings as inputs and obtain pRG equations for bilinear vertices which describe coupling of fermions to various order parameters introduced in the previous subsection. We will not consider all vertices with large/small momentum transfer in particle-hole and particle-particle channels and focus only on the ones which show the strongest divergencies. Once we obtain vertices, it will be straightforward to obtain susceptibilities. For convenience we summarize the interaction amplitudes in different channels in the Table I at the end of the section.

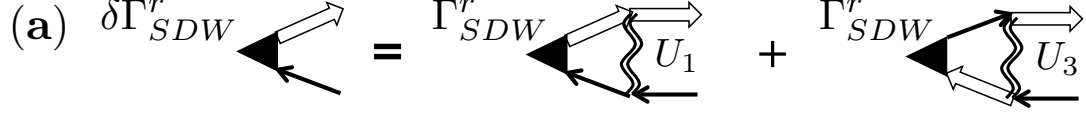
1. SDW channel

The SDW verices describe the coupling of fermions to SDW order parameters $\mathbf{s}_{1,2}^{r,i}$ and $\bar{\mathbf{s}}_{1,2}^{r,i}$, defined by Eqs. (98) and (99). The subscript 1,2 refers to the orbital, while the superscript r,i refers to a true SDW (real, r) or spin-current (imaginary, i) magnetic order. The order parameter $\mathbf{s}_{1,2}^r$, given by Eq. (98), is diagonal in orbital index and in real space describes the SDW magnetism of Fe atoms. The the order parameter $\bar{\mathbf{s}}_{1,2}^{r,i}$, given by Eq. (99), is off-diagonal in orbital index, and, when converted to real space, describes magnetism on pnictogen/chalcogen atoms rather than on Fe (Ref. [41]). We will refer to this order as off-diagonal spin polarization.

The order parameters in the orbital basis are $\mathbf{s}_1^{r,i} = d_{xz,\alpha}^\dagger \boldsymbol{\sigma}_{\alpha\beta} f_{xz,\beta} \pm f_{xz,\alpha}^\dagger \boldsymbol{\sigma}_{\alpha\beta} d_{xz,\beta}$ and $\bar{\mathbf{s}}_1^{r,i} = d_{xz,\alpha}^\dagger \boldsymbol{\sigma}_{\alpha\beta} f_{yz,\beta} \pm f_{xz,\alpha}^\dagger \boldsymbol{\sigma}_{\alpha\beta} d_{yz,\beta}$. In the band basis, $\mathbf{s}_1^{r,i} = \langle c_\alpha^\dagger \boldsymbol{\sigma}_{\alpha\beta} f_{1,\beta} \rangle \cos \theta + \langle d_\alpha^\dagger \boldsymbol{\sigma}_{\alpha\beta} f_{1,\beta} \rangle \sin \theta \pm \left(\langle f_{1,\alpha}^\dagger \boldsymbol{\sigma}_{\alpha\beta} c_\beta \rangle \cos \theta + \langle f_{1,\alpha}^\dagger \boldsymbol{\sigma}_{\alpha\beta} d_\beta \rangle \sin \theta \right)$, $\bar{\mathbf{s}}_1^{r,i} = \langle f_{1,\alpha}^\dagger \boldsymbol{\sigma}_{\alpha\beta} d_\beta \rangle \cos \theta - \langle f_{1,\alpha}^\dagger \boldsymbol{\sigma}_{\alpha\beta} c_\beta \rangle \sin \theta \pm \left(\langle c_\alpha^\dagger \boldsymbol{\sigma}_{\alpha\beta} f_{2,\beta} \rangle \cos \theta + \langle d_\alpha^\dagger \boldsymbol{\sigma}_{\alpha\beta} f_{2,\beta} \rangle \sin \theta \right)$, and analogous expressions for $\mathbf{s}_2^{r,i}$ and $\bar{\mathbf{s}}_2^{r,i}$. In all formulas the summation over small momenta near the corresponding E_F is implied with transferred momentum $(\pi, 0)$ for \mathbf{s}_1 and $(0, \pi)$ for \mathbf{s}_2 .

The pRG flow of the vertices is derived following the same procedure which we used to derive the pRG equations for the interactions [see Fig. 12(a)]

The equations decouple between diagonal and non-diagonal SDW vertices and between even real and imaginary order parameters. The interaction in the SDW channel with real order parameter, diagonal in the orbital index, is $-(U_1 + U_3)$ (see Eq. (101)), where U_1 and U_3 should be understood as running variables. We label the corresponding vertex as

(a) 

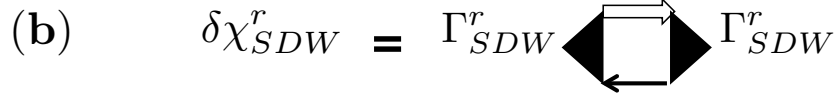
(b) 

FIG. 12: (a) The diagrammatic representation of the renormalization of the vertex Γ_{SDW}^r . The effective interaction in this channel is $U_1 + U_3$. (b) The diagrammatic representation of the flow equation for the spin susceptibility χ_{SDW}^r .

Γ_{SDW}^r In the Wilsonian computational scheme, the change in the SDW vertex due to the integration over the momenta k in the annulus between k and $k - \delta k$ is

$$d\Gamma_{SDW}^r = \frac{1}{2}\Gamma_{SDW}^r(U_1 + U_3) \int_{dk} \frac{d^2\mathbf{k}}{4\pi^2} \int \frac{d\epsilon}{2\pi} [G_{d_1;d_1}(i\epsilon, \mathbf{k})G_{f_1}(i\epsilon, \mathbf{k}) + G_{d_2;d_2}(i\epsilon, \mathbf{k})G_{f_2}(i\epsilon, \mathbf{k})] . \quad (115)$$

The prefactor of $1/2$ in Eq. (115) includes $1/8$ in Eq. (101), the factor of 2 due to the summation over two spin components, and the combinatorial factor of 2 obtained from two possible contractions with the two spin operators appearing in Eq. (101). Evaluating the momentum and frequency integrals we obtain

$$d\Gamma_{SDW}^r = \Gamma_{SDW}^r(U_1 + U_3) \frac{A}{4\pi} dL . \quad (116)$$

Expressing the interactions via dimensionless couplings, we re-write Eq. (116) as

$$\frac{d\Gamma_{SDW}^r}{dL} = \Gamma_{SDW}^r(u_1 + u_3/C) . \quad (117)$$

On the fixed trajectory, defined by Eqs. (90) and (93), Eq. (117) becomes

$$\frac{d\Gamma_{SDW}^r}{dL} = \Gamma_{SDW}^r u_1(1 + \gamma_3/C) . \quad (118)$$

where $u_1(L)$ is given by Eq. (83). Solving the differential equation, we obtain

$$\Gamma_{SDW}^r(L) = \Gamma_{SDW,0}^r \left(\frac{L_0}{L_0 - L} \right)^{\beta_{SDW}^r} , \quad (119)$$

where $\Gamma_{SDW,0}^r$ is of the same order as the bare SDW vertex, and

$$\beta_{SDW}^r = \frac{1 + \gamma_3/C}{1 + \gamma_3^2/C^2} . \quad (120)$$

The pRG flow of the spin susceptibility is shown in Fig. 12(b). It flows under pRG according to

$$\frac{d\chi_{SDW}^r}{dL} = (\Gamma_{SDW}^r)^2. \quad (121)$$

Solving this equation we obtain

$$\chi_{SDW}^r(L) \propto \frac{1}{(L_0 - L)^{\alpha_{SDW}^r}}, \quad (122)$$

where

$$\alpha_{SDW}^r = 2\beta_{SDW}^r - 1. \quad (123)$$

We see that the SDW spin susceptibility diverges at $L = L_0$, indicating the instability towards SDW magnetism, but only when $\alpha_{SDW}^r > 0$, i.e., when $\beta_{SDW}^r > 1/2$.

We emphasize that the present analysis does not resolve the orbital degeneracy of the SDW magnetism. Indeed the two observables, \mathbf{s}_1^r and \mathbf{s}_2^r defined in Eq. (98), describe the spin polarization of states made of xz and yz atomic orbitals respectively and the susceptibilities for the two order parameters are identical. Below the SDW instability, the coupling between these two order parameters determines whether they appear together or separately, i.e., whether SDW order is a stripe or a checkerboard.

The computation of the vertex and the susceptibility for the diagonal imaginary SDW order parameter (spin-current) proceeds in the same way, and the result is

$$\chi_{SDW}^i(L) \propto \frac{1}{(L_0 - L)^{\alpha_{SDW}^i}}, \quad (124)$$

where

$$\alpha_{SDW}^i = 2\beta_{SDW}^i - 1. \quad (125)$$

and

$$\beta_{SDW}^i = \frac{1 - \gamma_3/C}{1 + \gamma_3^2/C^2}. \quad (126)$$

This exponent is smaller than β_{SDW}^r , hence spin-current order is subleading to the real SDW order. The exponents, Eqs. (120), (123), (125), (126) are plotted as functions of the parameter $C = (m_e + m_h)/(2\sqrt{m_e m_h}) \geq 1$ in Fig. 13

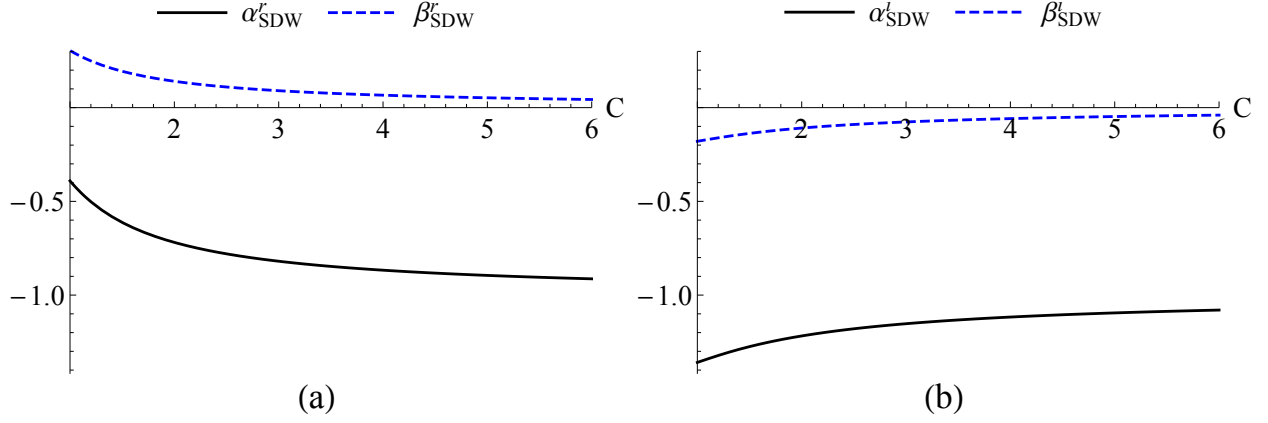


FIG. 13: The exponents α_{SDW}^r , β_{SDW}^r (a) and α_{SDW}^i , β_{SDW}^i (b) as functions of the parameter $C = (m_e + m_h)/(2\sqrt{m_e m_h}) \geq 1$.

Next, we consider the vertices for the coupling to other two order parameters $\bar{\mathbf{s}}_1^r$ and $\bar{\mathbf{s}}_2^r$, each with mixed orbital content. Using Eq. (101) and performing the same calculations as above, we find that the equations for the vertices with different orbital index decouple, and each $\bar{\Gamma}_{SDW}^r$ obeys

$$\frac{d\bar{\Gamma}_{SDW}^r}{dL} = \bar{\Gamma}_{SDW}^r(\bar{u}_1 + \bar{u}_3/C). \quad (127)$$

Because $u_{1,3} = \bar{u}_{1,3}$ on the fixed trajectory, see Eq. (88), the corresponding susceptibilities scale as

$$\bar{\chi}_{SDW}^r(L) \propto \frac{1}{(L_0 - L)^{\bar{\alpha}_{SDW}^r}} \quad (128)$$

has the same exponent as α_{SDW}^r , i.e., $\bar{\alpha}_{SDW}^r = \alpha_{SDW}^r$. This indicates that the spatial spin arrangement below the magnetic transition must include all four types of SDW order.

Similarly, the susceptibility $\bar{\chi}_{SDW}^r(L)$ behaves as

$$\bar{\chi}_{SDW}^i(L) \propto \frac{1}{(L_0 - L)^{\bar{\alpha}_{SDW}^i}}, \quad (129)$$

where along fixed trajectory $\bar{\alpha}_{SDW}^i = \alpha_{SDW}^i$.

2. CDW channel

The CDW order parameters are defined in Eq. (96) and Eq. (97). The corresponding interaction components are presented in Eq. (100).

The order parameters in the orbital basis are $\delta_1^{r,i} = d_{xz,\alpha}^\dagger f_{xz,\alpha} \pm f_{xz,\alpha}^\dagger d_{xz,\alpha}$ and $\bar{\delta}_1^{r,i} = d_{xz,\alpha}^\dagger f_{yz,\alpha} \pm f_{xz,\alpha}^\dagger d_{yz,\alpha}$. In the band basis, $\delta_1^{r,i} = \langle c_\alpha^\dagger f_{1,\alpha} \rangle \cos \theta + \langle d_\alpha^\dagger f_{1,\alpha} \rangle \sin \theta \pm (\langle f_{1,\alpha}^\dagger c_\alpha \rangle \cos \theta + \langle f_{1,\alpha}^\dagger d_\alpha \rangle \sin \theta)$, $\bar{\delta}_1^{r,i} = \langle f_{1,\alpha}^\dagger d_\alpha \rangle \cos \theta - \langle f_{1,\alpha}^\dagger c_\alpha \rangle \sin \theta \pm (\langle c_\alpha^\dagger f_{2,\alpha} \rangle \cos \theta + \langle d_\alpha^\dagger f_{2,\alpha} \rangle \sin \theta)$, and analogous expressions for $\delta_2^{r,i}$ and $\bar{\delta}_2^{r,i}$. Again, the summation over momentum is implied, the transferred momentum is $(\pi, 0)$ for δ_1 and $(0, \pi)$ for δ_2 .

The analysis of susceptibilities in the CDW channel is analogous to what we just did for the SDW channel and we skip intermediate steps. Along the fixed pRG trajectory the CDW susceptibilities for DCDW order parameters, diagonal in orbital index, scale as

$$\begin{aligned}\chi_{CDW}^r(L) &\propto \frac{1}{(L_0 - L)^{\alpha_{CDW}^r}} \\ \chi_{CDW}^i(L) &\propto \frac{1}{(L_0 - L)^{\alpha_{CDW}^i}},\end{aligned}\tag{130}$$

where the exponents are

$$\alpha_{CDW}^r = 2\beta_{CDW}^r - 1, \quad \alpha_{CDW}^i = 2\beta_{CDW}^i - 1\tag{131}$$

with

$$\begin{aligned}\beta_{CDW}^r &= \frac{1 - 2\gamma_2 - \gamma_3/C}{1 + \gamma_3^2/C^2} \\ \beta_{CDW}^i &= -\frac{1 - 2\gamma_2 + \gamma_3/C}{1 + \gamma_3^2/C^2}.\end{aligned}\tag{132}$$

The results Eq. (131) and (132) are presented graphically in Fig. 14.

For order parameters which are odd in the orbital index (anti-ferro-orbital order parameters) the susceptibilities along the fixed trajectory are

$$\begin{aligned}\bar{\chi}_{CDW}^r(L) &\propto \frac{1}{(L_0 - L)^{\bar{\alpha}_{CDW}^r}}, \\ \bar{\chi}_{CDW}^i(L) &\propto \frac{1}{(L_0 - L)^{\bar{\alpha}_{CDW}^i}}.\end{aligned}\tag{133}$$

The exponents $\bar{\alpha}_{CDW}^r$ and $\bar{\alpha}_{CDW}^i$ are the same as in the CDW channel, diagonal in the orbital index. One can verify this using Eq. (100) and the relation Eq. (88), i.e

$$\bar{\alpha}_{CDW}^r = \alpha_{CDW}^r, \quad \bar{\alpha}_{CDW}^i = \alpha_{CDW}^i.\tag{134}$$

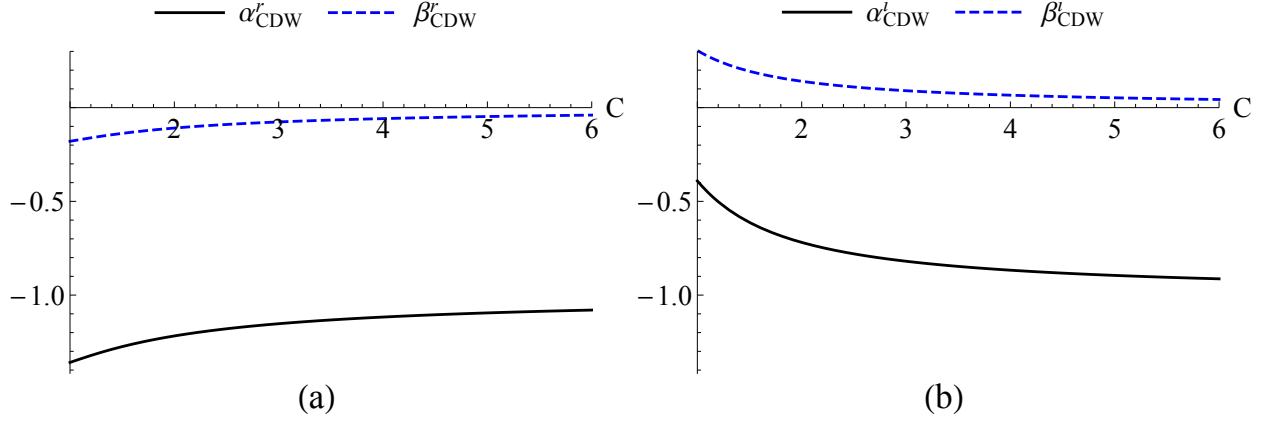


FIG. 14: (a) The exponents $\alpha_{CDW}^r, \beta_{CDW}^r$ and (b) $\alpha_{CDW}^i, \beta_{CDW}^i$ as functions of the parameter C .

3. Particle-particle channel

For simplicity, we will refer to the instability in the particle-particle channel as SC instability and to particle-particle channel as Cooper channel, although within our pRG this instability involves fermions with energies away from E_F and is towards the formation of a bound state of two fermions with zero total momentum.

We remind that there are three pairing channels with non-zero order parameters: A_{1g} , B_{1g} , and B_{2g} . The corresponding order parameters in the orbital basis are $\kappa_{A_1}^f = f_{xz,\uparrow}f_{xz,\downarrow} + f_{yz,\uparrow}f_{yz,\downarrow}$, $\kappa_{A_1}^d = d_{xz,\uparrow}d_{xz,\downarrow} + d_{yz,\uparrow}d_{yz,\downarrow}$, $\kappa_{B_1}^f = f_{xz,\uparrow}f_{xz,\downarrow} - f_{yz,\uparrow}f_{yz,\downarrow}$, $\kappa_{B_1}^d = d_{xz,\uparrow}d_{xz,\downarrow} - d_{yz,\uparrow}d_{yz,\downarrow}$, $\kappa_{B_2}^f = f_{xz,\uparrow}f_{yz,\downarrow} + f_{yz,\uparrow}f_{xz,\downarrow}$, $\kappa_{B_2}^d = d_{xz,\uparrow}d_{yz,\downarrow} + d_{yz,\uparrow}d_{xz,\downarrow}$. In the band basis, $\kappa_{A_1}^f = f_{1,\uparrow}f_{1,\downarrow} + f_{2,\uparrow}f_{2,\downarrow}$, $\kappa_{A_1}^d = c_{\uparrow}c_{\downarrow} + d_{\uparrow}d_{\downarrow}$, $\kappa_{B_1}^f = f_{1,\uparrow}f_{1,\downarrow} - f_{2,\uparrow}f_{2,\downarrow}$, $\kappa_{B_1}^d = (c_{\uparrow}c_{\downarrow} - d_{\uparrow}d_{\downarrow}) \cos 2\theta + (c_{\uparrow}d_{\downarrow} + d_{\uparrow}c_{\downarrow}) \sin 2\theta$, $\kappa_{B_2}^f = f_{1,\uparrow}f_{2,\downarrow} + f_{2,\uparrow}f_{1,\downarrow}$, $\kappa_{B_2}^d = (c_{\uparrow}c_{\downarrow} + d_{\uparrow}d_{\downarrow}) \sin 2\theta + (c_{\uparrow}d_{\downarrow} - d_{\uparrow}c_{\downarrow}) \cos 2\theta$. The summation over momenta is implied, the total momentum in each term is zero.

The running interactions in the B_{2g} channel, \tilde{U}_4 , $\tilde{\tilde{U}}_4$, \tilde{U}_5 , and $\tilde{\tilde{U}}_5$, all scale to zero, see Secs. II A and II B. In the other two channels, we introduce the vertices Γ_{C,A_1}^f and Γ_{C,A_1}^d for the coupling of fermions from electron and hole pockets to SC order parameter with A_{1g} symmetry, and Γ_{C,B_1}^f and Γ_{C,B_1}^d for the same in B_{1g} symmetry channel.

The pRG equations for these vertices are obtained using the same computational proce-

dure as before:

$$\begin{aligned} d\Gamma_{C,A_1(B_1)}^f &= -\Gamma_{C,A_1(B_1)}^f \frac{1}{2}(U_5 \pm \bar{U}_5) d\Pi_{C,A_1(B_1)}^f - \Gamma_{C,A_1(B_1)}^d \frac{1}{2}(U_3 \pm \bar{U}_3) d\Pi_{C,A_1(B_1)}^d \\ d\Gamma_{C,A_1(B_1)}^d &= -\Gamma_{C,A_1(B_1)}^f \frac{1}{2}(U_3 \pm \bar{U}_3) d\Pi_{C,A_1(B_1)}^f - \Gamma_{C,A_1(B_1)}^d \frac{1}{2}(U_4 \pm \bar{U}_4) d\Pi_{C,A_1(B_1)}^d, \end{aligned} \quad (135)$$

where the upper (lower) sign are for A_{1g} and B_{1g} channels, respectively. The quantities $d\Pi_{C,A_1(B_1)}^f$ and $d\Pi_{C,A_1(B_1)}^d$ are given by

$$\begin{aligned} d\Pi_{C,A_1(B_1)}^f &= \int_{dL} \frac{d^2k}{4\pi^2} \int \frac{d\epsilon}{2\pi} [G_{f_1}(i\epsilon, \epsilon_{f_1}(k)) G_{f_1}(-i\epsilon, -k) + G_{f_2}(i\epsilon, \epsilon_{f_1}(k)) G_{f_2}(-i\epsilon, -k)] \\ &= \frac{dL}{2\pi} A_e, \end{aligned} \quad (136)$$

and

$$\begin{aligned} d\Pi_{C,A_1(B_1)}^d &= \int_{dL} \frac{d^2k}{4\pi^2} \int \frac{d\epsilon}{2\pi} [G_{d_1,d_1}(i\epsilon, k) G_{d_1,d_1}(-i\epsilon, -k) + G_{d_2,d_2}(i\epsilon, k) G_{d_1,d_1}(-i\epsilon, -k) \\ &\quad \pm G_{d_1,d_2}(i\epsilon, k) G_{d_1,d_2}(-i\epsilon, -k) \pm G_{d_2,d_1}(i\epsilon, k) G_{d_2,d_1}(-i\epsilon, -k)] \\ &= \frac{dL}{2\pi} (A_h \pm A_h^-), \end{aligned} \quad (137)$$

In obtaining these expressions we used Eqs. (58), (62), (64), (60), (63), and (65). We show the equations for the interaction vertices graphically in Fig. 15.

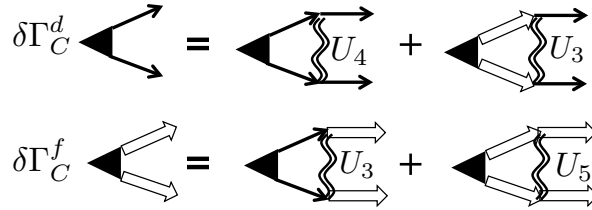


FIG. 15: The diagrammatic representation of the equations for the interaction vertices in the particle-particle channel. The contributions from \bar{U}_3 , \bar{U}_4 and \bar{U}_5 are not shown. They have the same structure as the ones we kept in the figure.

Substituting Eqs. (136) and (137) into Eq. (135), introducing dimensionless couplings, and approximating hole masses m_c and m_d as m_h , we obtain

$$\begin{aligned} \frac{d\Gamma_{C,A_1(B_1)}^f}{dL} &= -\Gamma_{C,A_1(B_1)}^f (u_5 \pm \bar{u}_5) - \Gamma_{C,A_1(B_1)}^d \frac{A_h}{AC} (u_3 \pm \bar{u}_3) \\ \frac{d\Gamma_{C,A_1(B_1)}^d}{dL} &= -\Gamma_{C,A_1(B_1)}^f \frac{A_e}{AC} (u_3 \pm \bar{u}_3) - \Gamma_{C,A_1(B_1)}^d (u_4 \pm \bar{u}_4). \end{aligned} \quad (138)$$

Along the stable fixed trajectory $u_i = \bar{u}_i$, hence the vertex in B_{1g} channel does not renormalize, while the one in A_{1g} channel obeys

$$\frac{d}{dL} \begin{bmatrix} \Gamma_{C,A_1}^f \\ \Gamma_{C,A_1}^d \end{bmatrix} = 2u_1 M_C \begin{bmatrix} \Gamma_{C,A_1}^f \\ \Gamma_{C,A_1}^d \end{bmatrix}, \quad M_C = \begin{bmatrix} |\gamma_4| & -\gamma_3 \frac{A_h}{AC} \\ -\gamma_3 \frac{A_e}{AC} & |\gamma_4| \end{bmatrix}. \quad (139)$$

Combining Γ_{C,A_1}^f and Γ_{C,A_1}^d into symmetric, s^{++} , and anti-symmetric, s^{+-} channels as

$$\begin{bmatrix} \Gamma_{C,A_1}^f \\ \Gamma_{C,A_1}^d \end{bmatrix} = \Gamma_{s^{+-}, s^{++}} \begin{bmatrix} \sqrt{A_h/A_e} \\ \mp 1 \end{bmatrix}, \quad (140)$$

where the upper and lower signs are for s^{+-} s^{++} channels, and using Eq. (71), we obtain from Eq. (139),

$$\frac{d\Gamma_{s^{+-}, s^{++}}}{dL} = 2u_1 (|\gamma_4| \pm \gamma_3) \Gamma_{s^{+-}, s^{++}}. \quad (141)$$

The exponent for the s^{+-} channel is obviously larger, and focusing on this channel only we obtain from (141)

$$\Gamma_{s^{+-}}(L) = \Gamma_{s^{+-}, 0} \left(\frac{L_0}{L_0 - L} \right)^{\beta_{s^{+-}}}, \quad (142)$$

where

$$\beta_{s^{+-}} = 2 \frac{|\gamma_4| + \gamma_3}{1 + \gamma_3^2/C^2}. \quad (143)$$

The pRG equation for the pairing susceptibility has the same form as in the SDW channel:

$$\frac{d\chi_{s^{+-}}}{dL} = \Gamma_{s^{+-}}^2. \quad (144)$$

Using Eq. (143) we obtain

$$\chi_{s^{+-}}(L) \propto \frac{1}{(L_0 - L)^{\alpha_{s^{+-}}}}, \quad (145)$$

where the exponent is

$$\alpha_{s^{+-}} = 2\beta_{s^{+-}} - 1 = 4 \frac{|\gamma_4| + \gamma_3}{1 + \gamma_3^2/C^2} - 1. \quad (146)$$

The exponents $\alpha_{s^{+-}}$ and $\beta_{s^{+-}}$ controlling the Cooper channel susceptibility and the vertex respectively are shown as functions of the parameter C in Fig. 16.

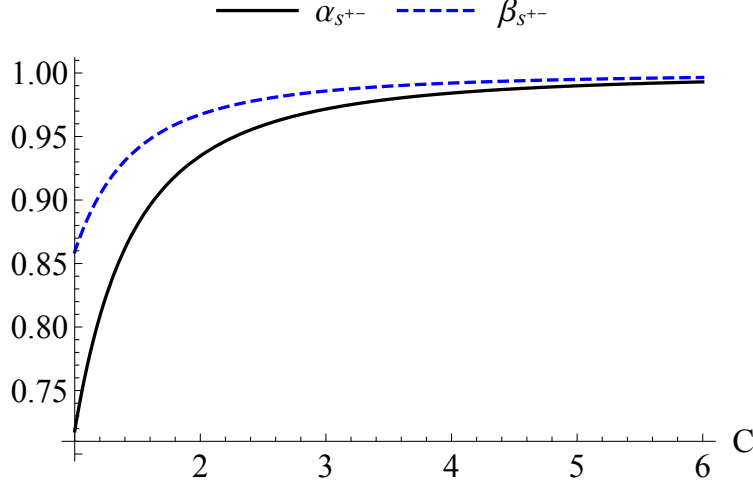


FIG. 16: The exponents α_{s+-} and β_{s+-} as functions of the parameter C . Both exponents approach 1 at large C .

As a side note, we remark that for the unstable fixed trajectory, Eq. (81), with $\bar{u}_i = 0$ for $i = 1 - 5$, the exponents in the A_{1g} and B_{1g} Cooper channels are identical. In both channels the superconducting susceptibilities scale as $\chi_{s+-} \approx \chi_{d+-} \propto 1/(L_0 - L)^{\alpha_{sc}}$ with $\alpha_{sc} = 2(|\gamma_4| + \gamma_3)/(1 + \gamma_3^2/C^2) - 1$.

We next compute susceptibilities in Pomeranchuk channels. There are four channels, even under inversion - A_1 , A_2 , B_1 and B_2 . The order parameters in these channels are presented in Eq. (109). We consider each channel separately.

4. B_1 Pomeranchuk channel

We first compute the vertex and the susceptibility in the B_1 charge Pomeranchuk channel. The corresponding order parameter in the orbital basis is $\rho_{B_1} = n_{xz} - n_{yz}$ with contributions from states near hole and electron pockets, $\rho_{B_1}^d$ and $\rho_{B_1}^f$, see Eq. (109). We label corresponding vertices as Γ_{ph,B_1}^d and Γ_{ph,B_1}^f . In the band basis, $\rho_{B_1}^d$ is the combination of $\langle c^\dagger c - d^\dagger d \rangle \cos 2\theta$ and $\langle c^\dagger d + d^\dagger c \rangle \sin 2\theta$ with equal amplitudes, while $\rho_{B_1}^f$ is just $\langle f_1^\dagger f_1 - f_2^\dagger f_2 \rangle$. As before, the summation over momentum is implied, the transferred momentum in all terms is equal to zero.

The polarization operator in the Pomeranchuk channel is not logarithmical and, moreover, internal and external energies are of the same order, i.e., if one probes the vertices Γ_{ph,B_1}^d

and Γ_{ph,B_1}^f at a scale L , typical internal scale in the diagram for vertex renormalization is also of order L . The vertex still flows logarithmically because its renormalization involves running interactions. However, because the running interaction in the B_{2g} Pomeranchuk channel is the only source of logarithmical flow, the ladder series of vertex renormalizations reduce to algebraic rather than differential equations for Γ_{ph,B_1}^d and Γ_{ph,B_1}^f . Using Eq. (112) for the vertices and evaluating ladder series of vertex renormalizations we obtain

$$\begin{bmatrix} \Gamma_{ph,B_1}^d \\ \Gamma_{ph,B_1}^f \end{bmatrix} = M_{B_1,ph} \begin{bmatrix} \Gamma_{ph,B_1}^d \\ \Gamma_{ph,B_1}^f \end{bmatrix} + \begin{bmatrix} \Gamma_{ph,B_1}^{d(0)} \\ \Gamma_{ph,B_1}^{f(0)} \end{bmatrix}, \quad (147)$$

where $\Gamma_{ph,B_1}^{d(0)}$ and $\Gamma_{ph,B_1}^{f(0)}$ are the bare vertices, and

$$M_{B_1,ph} = \begin{bmatrix} -2(u_4 - 2\tilde{u}_4 + \tilde{\tilde{u}}_4) & -2\frac{A_e}{A}(2u_1 - 2\bar{u}_1 - u_2 + \bar{u}_2) \\ -2\frac{A_h}{A}(2u_1 - 2\bar{u}_1 - u_2 + \bar{u}_2) & -2(u_5 - 2\tilde{u}_5 + \tilde{\tilde{u}}_5) \end{bmatrix}. \quad (148)$$

The relations Eq. (147) and (148) are illustrated in Fig. 17.

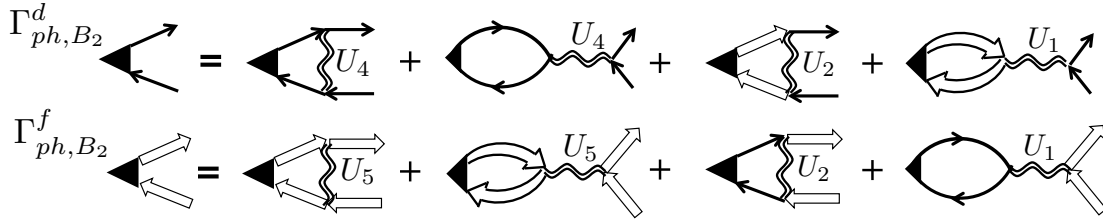


FIG. 17: The diagrammatic representation of the equations for the interaction vertices in B_1 Pomeranchuk channel. The contributions from \tilde{U}_4 , $\tilde{\tilde{U}}_4$, \bar{U}_1 and \bar{U}_2 are not shown. They have the same structure as the ones which we kept in the figure.

The two eigenvalues of the matrix $M_{B_1,ph}$ are

$$\begin{aligned} \lambda_{\pm}^{B_1} &= -(u_4 - 2\tilde{u}_4 + \tilde{\tilde{u}}_4 + u_5 - 2\tilde{u}_5 + \tilde{\tilde{u}}_5) \pm \sqrt{D_M}, \\ D_M &= (u_4 - 2\tilde{u}_4 + \tilde{\tilde{u}}_4 - u_5 + 2\tilde{u}_5 - \tilde{\tilde{u}}_5)^2 + 4C^2(2u_1 - 2\bar{u}_1 - u_2 + \bar{u}_2)^2 \end{aligned} \quad (149)$$

Along the stable fixed trajectory the two eigenvalues are degenerate:

$$\lambda_+^{B_1} = \lambda_-^{B_1} = \lambda^{B_1} = 2|\gamma_4|u_1 = \frac{2|\gamma_4|}{1 + \gamma_3^2 C^2} \frac{1}{L_0 - L}. \quad (150)$$

Accordingly,

$$\Gamma_{ph,B_1}^{d(f)} = \frac{\Gamma_{ph,B_1}^{d(0)(f(0))}}{1 - \lambda^{B_1}} \propto \frac{1}{L_{P_d} - L}, \quad (151)$$

where

$$L_{P_d} = L_0 - \frac{2|\gamma_4|}{1 + \gamma_3^2 C^2} \quad (152)$$

implies that B_1 Pomeranchuk vertices for states near hole and electron pockets grow independent on each other, each is proportional to its bare value. At $L \approx L_{P_d}$, when the running $\Gamma_{ph,B_1}^{d(f)}$ are much larger than their bare values, the ratio $\Gamma_{ph,B_1}^d/\Gamma_{ph,B_1}^f$ actually tends to a universal number, determined by the way how the system approaches the fixed trajectory. Solving for the ratio $\Gamma_{ph,B_1}^d/\Gamma_{ph,B_1}^f$ by setting $\Gamma_{ph,B_1}^{d(0)(f(0))}$ to zero but keeping $u_i - \bar{u}_i$ small but finite, we obtain from (147) and (149) that $\Gamma_{ph,B_1}^d/\Gamma_{ph,B_1}^f$ approaches 4 at $L = L_0$. We cited this result in the main text.

The B_1 Pomeranchuk susceptibility is given by a series of diagrams which consist of a particle-hole bubble with ladder series of vertex renormalizations. Because integration over internal momenta in each cross-section does not give rise to logarithms, ladder renormalizations can be absorbed into the renormalization of just one of side vertices. As a result,

$$\chi_{ph,B_1} \sim \Gamma_{ph,B_1}^{d(f)} \propto \frac{1}{L_{P_d} - L}. \quad (153)$$

We see that Pomeranchuk susceptibility diverges with the exponent $\alpha_{P_d} = 1$ and, moreover, $L_{P_d} < L_0$, i.e., Pomeranchuk susceptibility diverges at a smaller L (i.e., at a larger temperature) than the susceptibilities in SDW and SC channels. We discuss the consequences in the main text.

We emphasize the role of the flow of the couplings plays the major role in this analysis. If we did the same calculation as above but with the bare couplings related to Hund and Hubbard interaction terms, we would obtain

$$M_{ph,B_1} = -(U - 2U' + J) \frac{m}{2\pi} \begin{bmatrix} 1 & 1 \\ 1 & 1 \end{bmatrix}. \quad (154)$$

For simplicity we set $m_e = m_h = m$. The matrix M_{ph,B_1} has one zero eigenvalue $\lambda_- = 0$ due to the particle-hole symmetry at the bare level, and the other one is $\lambda_+ = -(U - 2U' + J) \frac{m}{2\pi}$. This eigenvalue is positive only when $U' > (U + J)/2$, and, even if it is positive, $2U' - (U + J)$ has to exceed the critical value, otherwise the Pomeranchuk instability does not develop. In the full theory, which incorporates the flow of the couplings, the Pomeranchuk instability develops at arbitrary Hubbard and Hund repulsive interactions and for arbitrary ratios of U, U' and J .

5. A_1 channel

The Pomeranchuk susceptibility in the A_1 channel is analysed in a similar way. The A_1 order parameter in the orbital basis is $\rho_{A_1} = n_{xz} + n_{yz}$ with contributions from states near hole and electron pockets, $\rho_{A_1}^d$ and $\rho_{A_1}^f$, see Eq. (109). We label corresponding vertices as Γ_{ph,A_1}^d and Γ_{ph,A_1}^f . In the band basis, $\rho_{A_1}^d$ is $\langle c^\dagger c + d^\dagger d \rangle$ and $\rho_{A_1}^f$ is $\langle f_1^\dagger f_1 + f_2^\dagger f_2 \rangle$. By analogy with superconductivity, we label the state with the same sign of $\rho_{A_1}^d$ and $\rho_{A_1}^f$ as s^{++} and the state with opposite signs as s^{+-} .

The interaction in the A_1 channel is presented in Eq. (111). Using this equation and performing the same analysis as in the B_2 channel, we find the set of self-consistent equations for A_1 vertices in the form

$$\begin{bmatrix} \Gamma_{ph,A_1}^d \\ \Gamma_{ph,A_1}^f \end{bmatrix} = M_{A_1,ph} \begin{bmatrix} \Gamma_{ph,A_1}^d \\ \Gamma_{ph,A_1}^f \end{bmatrix} + \begin{bmatrix} \Gamma_{ph,A_1}^{d(0)} \\ \Gamma_{ph,A_1}^{f(0)} \end{bmatrix}, \quad (155)$$

where $\Gamma_{ph,A_1}^{d(0)}$ and $\Gamma_{ph,A_1}^{f(0)}$ are the bare vertices, and

$$M_{A_1,ph} = \begin{bmatrix} -2(u_4 + 2\tilde{u}_4 - \tilde{\tilde{u}}_4) & -2\frac{A_e}{A}(2u_1 + 2\bar{u}_1 - u_2 - \bar{u}_2) \\ -2\frac{A_h}{A}(2u_1 + 2\bar{u}_1 - u_2 - \bar{u}_2) & -2(u_5 + 2\tilde{u}_5 - \tilde{\tilde{u}}_5) \end{bmatrix}. \quad (156)$$

The two eigenvalues of the matrix $M_{A_1,ph}$ are

$$\begin{aligned} \lambda_{\pm}^{A_1} &= -(u_4 + 2\tilde{u}_4 - \tilde{\tilde{u}}_4 + u_5 + 2\tilde{u}_5 - \tilde{\tilde{u}}_5) \pm \sqrt{D_M}, \\ D_M &= (u_4 + 2\tilde{u}_4 - \tilde{\tilde{u}}_4 - u_5 - 2\tilde{u}_5 + \tilde{\tilde{u}}_5)^2 + 4C^2(2u_1 + 2\bar{u}_1 - u_2 - \bar{u}_2)^2 \end{aligned} \quad (157)$$

These two eigenvalues are not degenerate along the stable fixed trajectory, Eq. (88), and are given by

$$\lambda_{\pm}^{A_1} = 2(|\gamma_4| \pm 4C)u_1. \quad (158)$$

It follows from Eq. (155) that $\lambda_+^{A_1}$ is the effective coupling in s^{+-} channel and $\lambda_-^{A_1}$ is the effective coupling in s^{++} channel. The coupling in the s^{+-} channel is obviously larger and below we focus only on this channel. The corresponding susceptibility scales as

$$\chi_{A_1}^{s^{+-}} \propto \frac{1}{L_{P_s} - L}, \quad (159)$$

where

$$L_{P_s} = L_0 - \frac{2(|\gamma_4| + 4C)}{1 + \gamma_3^2 C^2}. \quad (160)$$

In our model the instability in A_1 channel occurs prior to the instability in B_2 channel, but in a generic three-orbital low-energy model B_2 instability well may come first.

In physical terms, A_1 , s^{+-} order leads to opposite shifts in the chemical potentials for electrons and holes. This does not break any symmetry, and the opposite shift of μ_h and μ_e can be obtained from fermionic self-energy (which is neglected in RG analysis). Because no symmetry is broken, there will be no true instability in A_1 channel once effects beyond pRG are included. Still, at some distance from L_{P_s} the A_1 susceptibility obeys Eq. (159), what in practice mean that the separation between μ_e and μ_h grows as the temperature approaches the one which corresponds to $L = L_{P_s}$ (we recall that L can be interpreted as $\log W/T$, where W is of order bandwidth).

We again emphasize the role of the flow of the couplings. If we used the bare interactions instead of the running ones, we would obtain the matrix $M_{A_1,ph}$ in the form,

$$M_{A_1,ph} = -(U + 2U' - J) \frac{m}{2\pi} \begin{bmatrix} 1 & 1 \\ 1 & 1 \end{bmatrix}. \quad (161)$$

As a result, $\chi_+^{A_1} \propto J - (U + 2U')$ and it would be negative for realistic U, U' , and J . This implies that the increase of the susceptibility in A_1 s^{+-} channel is entirely due to the flow of the couplings.

6. A_2 and B_2 channels

The A_2 order parameter in the orbital basis is $\rho_{A_2}^d = d_{xz}^\dagger d_{yz} - d_{yz}^\dagger d_{xz}$, $\rho_{A_2}^f = f_{xz}^\dagger f_{yz} - f_{yz}^\dagger f_{xz}$, see Eq. (109). In the band basis, $\rho_{A_2}^d = \langle c^\dagger d - d^\dagger c \rangle$ and $\rho_{B_2}^f$ is $\langle f_1^\dagger f_2 - f_2^\dagger f_1 \rangle$. The B_2 order parameter in the orbital basis is $\rho_{B_2}^d = d_{xz}^\dagger d_{yz} + d_{yz}^\dagger d_{xz}$ and $\rho_{B_2}^f = f_{xz}^\dagger f_{yz} + f_{yz}^\dagger f_{xz}$. In the band basis, $\rho_{B_2}^d = \langle c^\dagger d + d^\dagger c \rangle \cos 2\theta + \langle d^\dagger d - c^\dagger c \rangle \sin 2\theta$ and $\rho_{B_2}^f$ is $\langle f_1^\dagger f_2 + f_2^\dagger f_1 \rangle$.

The computation of susceptibilities in these two channels proceeds in the same way as for A_1 and B_1 channels. The vertices Γ_{A_2, B_2}^f do not renormalize because one of energies in the bubble made out of f_1 and f_2 fermions is necessary large. The vertices Γ_{A_2, B_2}^d do renormalize, and along the fixed trajectory we obtained $\Gamma_{A_2, B_2}^d = \Gamma_{A_2, B_2}^{d,0} / (1 - \lambda_{A_2, B_2})$, with

$$\lambda_{A_2, B_2} = |\gamma_4| u_1. \quad (162)$$

Accordingly, the susceptibilities in these two channels scale as

$$\chi_{A_2, B_2} \propto \frac{1}{L_{P'_{s,d}} - L}, \quad (163)$$

where

$$L_{P'_{s,d}} = L_0 - \frac{|\gamma_4|}{1 + \gamma_3^2 C^2}. \quad (164)$$

Comparing this form with critical L in A_1 and B_1 channels, we see that $L_{P'_{s,d}} > L_{P_d}$. As the result, the susceptibilities in A_2 and B_2 channels diverge at a lower T than the one in B_1 channel, hence these channels are subleading to B_1 channel. plot $L_0 - L_{P_d}$, $L_0 - L_{P_s}$, and $L_0 - L_{P'_{sd}}$ as functions of C in Fig. 18.

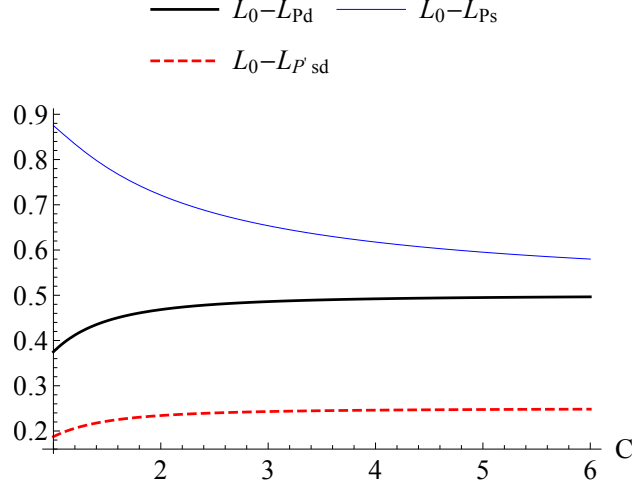


FIG. 18: The differences $L_0 - L_{P_d}$, $L_0 - L_{P_s}$, and $L_0 - L_{P'_{sd}}$ as functions of the parameter C . L_{P_s} , L_{P_d} and $L_{P'_{sd}}$ are the values of L at which Pomeranchuk susceptibilities in A_1 , B_1 , and A_2/B_2 channels diverge within RG. The larger in the difference, the larger is the temperature at which the instability occurs. The divergence of the susceptibility in A_1 channel is an artefact of RG approximation as it does not give rise to a symmetry breaking. This divergence is cut by terms not included into one-loop RG. The divergence in the B_1 channel is the real one, and leads to d -wave orbital order.

V. THE MODEL WITH d_{xy} ELECTRON POCKETS.

For completeness, we also analyzed the model in which we approximated the two electron pockets as purely d_{xy} . In this approximation, inter-orbital Hubbard interaction acts within the subset of the two hole pockets, which, like before, are made out of d_{xz} and d_{yz} orbitals, and within the subset of the two electron pockets. The corresponding interaction terms are U_4 , U_5 , \bar{U}_5 , \tilde{U}_5 , $\tilde{\tilde{U}}_5$ terms in Eq. (19). The bare values of all these couplings are Hubbard

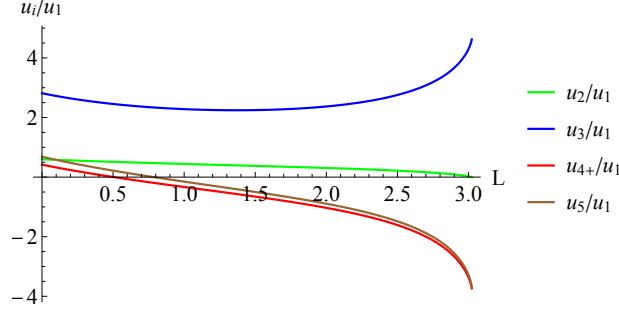


FIG. 19: The solution of the pRG equations, Eqs. (172), for the model where the electron pockets have d_{xy} orbital content. The pRG equations and the fixed trajectory are the same as in the model with d_{xz}/d_{yz} electron pockets, however initial values of the couplings are different. The convergence towards the fixed trajectory is much better for d_{xy} electron pockets.

U , i.e.,

$$U_{4,0} = U_{5,0} = \bar{U}_{5,0} = \tilde{U}_{5,0} = \tilde{\tilde{U}}_{5,0} = U. \quad (165)$$

Inter-orbital Hubbard terms include density-density interactions U_1 and \bar{U}_1 between hole and electron pockets and interaction \tilde{U}_4 within d_{xz} and d_{yz} components of hole pockets. Because d_{xy} orbital interacts equally with d_{xz} and d_{yz} orbitals, the bare value of U_1 and \bar{U}_1 are equal, i.e.,

$$U_{1,0} = \bar{U}_{1,0} = \tilde{U}_{4,0} = U'. \quad (166)$$

The exchange Hund interaction J acts in the subspace of d_{xz} and d_{yz} orbitals ($\tilde{\tilde{U}}_4$ term) and between d_{xy} and d_{xz}/d_{yz} orbitals (U_2 and \bar{U}_2 terms). Again, d_{xy} orbital interacts equally with d_{xz} and d_{yz} orbitals, hence the bare values of U_2 and \bar{U}_2 are equal:

$$U_{2,0} = \bar{U}_{2,0} = \tilde{\tilde{U}}_{4,0} = J. \quad (167)$$

Finally, pair-hopping interaction J' also acts in the subspace of d_{xz} and d_{yz} orbitals (\bar{U}_4 term) and between d_{xy} and d_{xz}/d_{yz} orbitals (U_3 and \bar{U}_3 terms). Like for other interactions, bare values of U_3 and \bar{U}_3 are equal:

$$U_{3,0} = \bar{U}_{3,0} = \bar{U}_{4,0} = J'. \quad (168)$$

The structure of low-energy electronic states is the same as in the model which we considered in the main text, hence pRG equations are the same as in (74). The couplings \tilde{U}_4 and $\tilde{\tilde{U}}_4$ still flow to zero if the bare \tilde{U}_4 exceeds the bare $\tilde{\tilde{U}}_4$, which is the case when $U' > J$. The

couplings \tilde{U}_5 and $\tilde{\bar{U}}_5$ remain equal under pRG, and both tend to zero when $U > 0$. One can further make sure that the couplings u_1 and \bar{u}_1 , u_2 and \bar{u}_2 , u_3 and \bar{u}_3 , u_5 and \bar{u}_5 , which are equal at the bare level, remain equal under pRG. This reduces the set of pRG equations to

$$\begin{aligned}
\dot{u}_1 &= u_1^2 + u_3^2/C^2 \\
\dot{u}_2 &= 2u_1u_2 - 2u_2^2 \\
\dot{u}_3 &= -u_3(u_4 + \bar{u}_4) + 4u_3u_1 - 2u_2u_3 - 2u_5u_3 \\
\dot{u}_4 &= -u_4^2 - \bar{u}_4^2 - 2u_3^2 \\
\dot{\bar{u}}_4 &= -2u_4\bar{u}_4 - 2u_3^2 \\
\dot{u}_5 &= -2u_5^2 - 2u_3^2
\end{aligned} \tag{169}$$

The transformation from U_i to dimensionless u_i is the same as before, and we remind that $C = (m_e + m_h)/2\sqrt{m_em_h}$.

Introducing $u_{4+} = (u_4 + \bar{u}_4)/2$ and $u_{4-} = (u_4 - \bar{u}_4)/2$ we immediately find that the equation for u_{4-} decouples from the rest:

$$\dot{u}_{4-} = -u_{4-}^2, \tag{170}$$

i.e.,

$$u_{4-} = \frac{u_{4-,0}}{1 + u_{4-,0}L}. \tag{171}$$

At the bare level, $u_{4-,0} > 0$. Eq. (171) then shows that u_{4-} tends to zero under pRG. The other equations become

$$\begin{aligned}
\dot{u}_1 &= u_1^2 + u_3^2/C^2 \\
\dot{u}_2 &= 2u_1u_2 - 2u_2^2 \\
\dot{u}_3 &= -2u_3u_{4+} + 4u_3u_1 - 2u_2u_3 - 2u_5u_3 \\
\dot{u}_{4+} &= -2u_{4+}^2 - 2u_3^2 \\
\dot{u}_5 &= -2u_5^2 - 2u_3^2.
\end{aligned} \tag{172}$$

The fixed trajectory for these equations is the same as for the model with d_{xz}/d_{yz} electron pockets, namely $u_i = \bar{u}_i$, $u_2/u_1 = 0$, $u_3 = \gamma_3u_1$, $u_4 = u_5 = \gamma_4u_1$, where $\gamma_3 = C\sqrt{8C^2 - 1 + 4\sqrt{1 - C^2 + 4C^4}}$, $\gamma_4 = 1 - 2C^2 - \sqrt{1 - C^2 + 4C^4}$, and

$$u_1 = \frac{1}{1 + \left(\frac{\gamma_3}{C}\right)^2} \frac{1}{L_0 - L}. \tag{173}$$

However, because $u_i = \bar{u}_i$, $i = 1, 2, 3$ already at the bare level, the system approaches the fixed trajectory faster than in the model which we studied in the main text. We show pRG flow of the ratios of the couplings in Fig. 19.